Does ERA5 Mark a New Era for Resolving the Tropical Cyclone Environment?

Christopher J. Slocum,[a] Muhammad Naufal Razin,[b] John A. Knaff,[a] and Justin P. Stow[c]

[a] *NOAA Center for Satellite Research and Applications, Fort Collins, Colorado*
[b] *Cooperative Institute for Research in the Atmosphere, Colorado State University, Fort Collins, Colorado*
[c] *Department of Meteorology and Atmospheric Science, The Pennsylvania State University, University Park, Pennsylvania*

ABSTRACT: The synoptic environment around tropical cyclones plays a significant role in vortex evolution. To capture the environment, the operational and research communities calculate diagnostic quantities. To aid with applications and research, the Tropical Cyclone Precipitation, Infrared, Microwave, and Environmental Dataset (TC PRIMED) combines disparate data sources. A key part of TC PRIMED is the environmental context. Often, environmental diagnostics come from multiple sources. However, TC PRIMED uses the European Centre for Medium-Range Weather Forecasts fifth-generation reanalysis (ERA5) product to provide a more complete representation of the storm environment from a single source. Reanalysis products usually poorly resolve tropical cyclones and their surrounding environment. To understand the uncertainty of large-scale diagnostics, ERA5 is compared to the Statistical Hurricane Intensity Prediction Scheme developmental dataset and the National Oceanic and Atmospheric Administration Gulfstream IV-SP dropwindsondes. This analysis highlights biases in the ERA5 environmental diagnostic quantities. Thermodynamic fields show the largest biases. The boundary layer exhibits a cold temperature bias that limits the amount of convective instability; also, the upper troposphere contains temperature biases and shows a high relative humidity bias. However, the upper-troposphere large-scale kinematic fields and derived metrics are low biased. In the lower troposphere, the temperature gradient and advection calculated from the thermal wind suggest that the low-level wind field is not representative of the observed distribution. These diagnostics comparisons provide uncertainty so that users of TC PRIMED can assess the implications for specific research and operational applications.

KEYWORDS: Tropical cyclones; Hurricanes/typhoons; Dropsondes; Diagnostics; Reanalysis data

1. Introduction

The multiscale nature of tropical cyclones poses a challenge to understanding the interplay between factors that influence hazards and impacts. Often to simplify the complex relationships, the tropical cyclone research community either focuses on the "mesoscale power plant" or the "synoptic-scale supporting structure" (Ooyama 1982). Through improving our overall understanding, the community has made considerable progress in developing skillful operational statistical–dynamical guidance and mesoscale tropical cyclone models. However, challenges remain in understanding and forecasting aspects of the tropical cyclone (e.g., tropical cyclogenesis, the tail of the distribution of intensity change, and secondary eyewall formation and eyewall replacement). To assist with analysis of these events in global tropical cyclones, Razin et al. (2022a,b) created a new dataset that combines satellite observations and derived products called the Tropical Cyclone Precipitation,

Infrared, Microwave, and Environmental Dataset (TC PRIMED). TC PRIMED contains global tropical cyclone–centric 1) intercalibrated, low-Earth-orbiter passive microwave brightness temperatures, 2) NASA's Goddard Profiling Algorithm retrieved rainfall, 3) geostationary satellite long-wave window channel infrared brightness temperatures and derived metrics, 4) tropical cyclone position and intensity, and 5) NASA's Tropical Rainfall Measuring Mission and Global Precipitation Measurement Core Observatory satellite precipitation radar observations. In addition, TC PRIMED includes storm-centric, large-scale environmental diagnostic quantities. To calculate these diagnostics from a consistent source, TC PRIMED uses the European Centre for Medium-Range Weather Forecasts (ECMWF) fifth-generation reanalysis product (ERA5; Hersbach and Dee 2016; Hersbach et al. 2020). Here, we discuss deriving these diagnostics.

Model reanalysis products aid in dissecting atmospheric processes through combining a consistent model dynamical core and physics parameterizations with the best available conventional and satellite-based observations through data assimilation (Kalnay 2003). However, because of the computational cost, the horizontal resolution of these products is coarser than the operational or parent model equivalent. As a result, reanalysis can lack the ability to resolve certain tropical cyclone processes, especially at storm scale, impacting the usefulness and applicability of a reanalysis product (Hodges et al. 2017). Here, we focus on how well the reanalysis synoptic-scale supporting structure represents the storm environment in observational datasets. We use dropwindsondes from the

---

ᵒ Denotes content that is immediately available upon publication as open access.

🖉 Supplemental information related to this paper is available at the Journals Online website: https://doi.org/10.1175/JCLI-D-22-0127.s1.

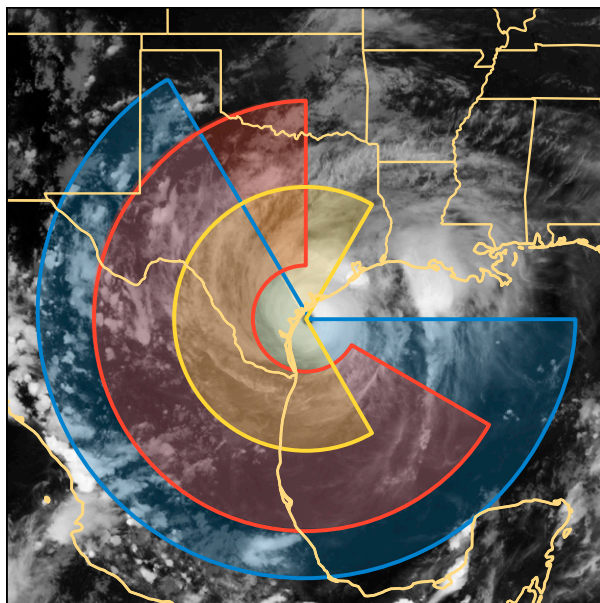*Corresponding author*: Chris Slocum, christopher.slocum@noaa.gov

FIG. 1. *GOES-16* preliminary, nonoperational 10.3-μm longwave infrared observation at 0000 UTC 26 Aug 2017 showing Hurricane Harvey prior to landfall with the area-averaging regions for large-scale dynamics from 0 to 1000 km (blue circle), thermodynamics from 200 to 800 km (red annulus), and kinematics from 0 to 500 km (yellow circle). Note that portions of each circle and annulus are removed to assist with clarity.

North Atlantic and eastern and central North Pacific to evaluate quantities in the modeled large-scale environment.

What defines the large-scale environment around a tropical cyclone depends on the purpose and can be specific to an atmospheric state variable. With total kinetic energy, Ooyama (1969) shows the impact of the inner core on the size metric when using a radius inside 500 km. And, in his simulations, the tropical cyclone induces a response as far as 1000 km [Fig. 10 in Ooyama (1969)]. Through composite analyses of rawinsondes, Frank (1977) demonstrates that temperature perturbations induced by the tropical cyclone vortex extend out to 14°–15° latitude from the storm center. For factors that influence storm evolution, other near-storm quantities are useful. Hill and Lackmann (2009) show how near-storm moisture affects the changes to storm size; also, the community has documented the impacts of shear and dry-air entrainment on tropical cyclone formation, intensity, and rapid intensity change (e.g., Gray 1979). Quantities such as temperature gradient and advection provide insight into the baroclinic environment through measuring warm and cold air advection around the storm and provide insight into storm intensification and growth (Maclay et al. 2008). To capture tropical cyclone and environment interactions, statistical–dynamical intensity forecast aids use model-derived, area-averaged quantities. Figure 1 shows Hurricane Harvey in *GOES-16* longwave infrared imagery at 0000 UTC 26 August 2017 before landfall and the three regions used by statistical–dynamical aids such as the Statistical Hurricane Intensity Prediction Scheme (SHIPS; DeMaria and Kaplan 1994), Logistic Growth Equation Model

(DeMaria 2009), Tropical Cyclone Formation Probability product (Schumacher et al. 2009), and Rapid Intensification Prediction Aid (Knaff et al. 2018). These aids average large-scale dynamic quantities like vorticity and divergence in the storm-centric region from 0 to 1000 km in radius (blue circle), thermodynamic quantities like temperature and relative humidity in an annulus from 200 to 800 km (red annulus), and kinematic (e.g., wind) quantities from 0 to 500 km (yellow circle).

To include this familiar representation of the environment in TC PRIMED, we use these area-averaging definitions to calculate large-scale environmental diagnostic quantities from the ERA5 product output. We opt for ERA5 over the SHIPS developmental dataset to provide full vertical profiles of dynamic, kinematic, and thermodynamic variables in addition to derived metrics. Also, in using ERA5, we limit the source of the diagnostics to a singular, consistent source over the 1998–2019 period of the satellite observations in TC PRIMED. In addition to outlining the calculations, we discuss errors in context with observations. We believe that this context provides critical information on the uncertainties and potential limitations of these quantities for research and forecast applications for either the SHIPS developmental dataset—the classic source for these data—or the large-scale environmental diagnostic quantities from ERA5 in TC PRIMED. For this manuscript, we outline the datasets including ERA5, storm characteristics, the SHIPS developmental dataset (DeMaria et al. 2005) and dropwindsonde observations in section 2. Then, we discuss the methods for calculating large-scale environmental profiles and diagnostic quantities in section 3. We provide a comparison between ERA5 diagnostics and the SHIPS developmental dataset in section 4 before comparing ERA5 diagnostics to observations in section 5. In section 6, we offer a discussion of ERA5-based large-scale environmental diagnostics for tropical cyclones.

2. Data

We use 1) the ECMWF reanalysis version 5 pressure-level and single-level products to calculate storm-relative large-scale environmental diagnostic quantities, 2) the Automated Tropical Cyclone Forecast system database for storm characteristics, 3) the SHIPS developmental dataset for comparison, and 4) National Oceanic and Atmospheric Administration (NOAA) Gulfstream IV-SP N49RF synoptic dropwindsondes to understand vertical kinematic and thermodynamic errors.

a. ECMWF reanalysis version 5

For the ECMWF fifth-generation reanalysis product (ERA5; Hersbach and Dee 2016; Hersbach et al. 2020), ECMWF uses the Integrated Forecast System cycle 41r2 at triangular truncation number 639 (approximately 31-km horizontal resolution) with 137 hybrid sigma vertical levels. ECMWF makes reanalysis output available on pressure- and single-level surfaces at a uniform 0.25° horizontal resolution through the European Union's Copernicus Climate Change Service (Hersbach et al. 2018a,b). For the reanalysis product, the four-dimensional variational-analysis data assimilation uses 12-h windows centered at

TABLE 1. ERA5 single-level (top section) and pressure-level (middle section) data and bounding radii for area average. Derived quantities calculated from the single- and pressure-level data are in the bottom section.

Quantity	Units	Area averaging (km)
Single-level data		
u and v wind at 10 m	m s^{-1}	0–500 and 200–800
Temperature at 2 m	K	0–500 and 200–800
Dewpoint temperature at 2 m	K	0–500 and 200–800
Sea surface temperature	K	0–50
Precipitable water	mm	Multiple radii
Pressure-level data		
u and v wind	m s^{-1}	0–500 and 200–800
Temperature	K	0–500 and 200–800
Relative humidity	%	0–500 and 200–800
Specific humidity	kg kg^{-1}	0–500 and 200–800
Geopotential height	m	0–500 and 200–800
Divergence	s^{-1}	0–1000
Relative vorticity	s^{-1}	0–1000
Derived quantities		
Deep-layer and generalized shear	m s^{-1}	0–500 and 200–800
Temperature gradient	°C m^{-1}	0–500 and 200–800
Temperature advection	°C s^{-1}	0–500 and 200–800
Convective mass flux	m s^{-1}	0–500 and 200–800

0300 and 1500 UTC to produce hourly analyses and initialize 18-h forecasts twice daily starting at 0600 and 1800 UTC.

Here, we use the hourly analysis product at synoptic times (i.e., 0000, 0600, 1200, and 1800 UTC). We subset pressure-level data from 100 to 1000 hPa at 50-hPa intervals with the addition of 925 and 975 hPa. For pressure-level fields, we use the temperature, relative humidity, specific humidity, zonal and meridional components of the wind, geopotential (converted to geopotential height), relative vorticity, and divergence. From the single-level data, we take the precipitable water, large-scale and convective rain rates, sea surface temperature, mean sea level pressure, 2-m temperature and dewpoint temperature, and 10-m zonal and meridional wind components. We list a summary of these output fields in Table 1.

b. Automated tropical cyclone forecast system database

The Automated Tropical Cyclone Forecast (ATCF; Sampson and Schrader 2000) system combines working and postseason tropical cyclone characteristic data from the National Hurricane Center, Central Pacific Hurricane Center, and Joint Typhoon Warning Center. For this work, we extract the 6-h position (i.e., storm center longitude and latitude), maximum sustained one-minute average wind or intensity, central minimum pressure, and development level (e.g., disturbance, open wave, tropical storm, tropical cyclone, extratropical) from the best-track database files for the 1998–2019 seasons for the North Atlantic, the western, central, and eastern North Pacific, the north Indian Ocean, and the Southern Hemisphere tropical cyclone basins. While commonly used in tropical cyclone applications, the best-track dataset contains values at 0.1° and 5-kt resolution (1 kt ≈ 0.51 m s^{-1}) for track and intensity, respectively. In addition to resolution, the quantities in the best-track database have uncertainty caused by data available to discern the quantity of interest (Torn and Snyder 2012; Landsea and Franklin 2013; Combot et al. 2020).

c. SHIPS developmental dataset

Operational statistical–dynamical forecast aids use the SHIPS developmental dataset (RAMMB 2022) to represent the large-scale environment with parameters endemic to tropical cyclone intensity change. This information amalgamates current observations with model output products. In the operational versions of the large-scale diagnostics, the algorithm uses the working best-track position and official forecast track of the tropical cyclone, available geostationary infrared imagery, current satellite-based ocean temperature analysis, and forecast fields from the operational version of the Global Forecast System. For the developmental dataset, Cooperative Institute for Research in the Atmosphere (CIRA) and Regional and Mesoscale Meteorology Branch (RAMMB) take observational data that may have been missing in real time and combine them with the final best track to create a more realistic estimate of the storm environment for tropical systems. CIRA and RAMMB do not produce developmental dataset output at synoptic periods for systems that do not have final best tracks (at least tropical depression intensity) or systems that are nontropical (e.g., extratropical and subtropical). For the model fields, CIRA and RAMMB apply a perfect prognostic approach with model analyses and reanalyses (DeMaria et al. 2005). In the current version of the developmental dataset, CIRA and RAMMB use 1° × 1° model data from the Climate Forecast System Reanalysis from 1982 to 1999 and the Global Forecast System analyses from 2000 to present (RAMMB 2022). Here, we use 200–800-km temperature, relative humidity, and convective mass flux and 0–500-km wind, vertical wind shear, and temperature gradient and advection.

d. Dropwindsonde

Since 1997 in support of operations and research for tropical cyclones, the NOAA Gulfstream IV-SP N49RF (G-IV) releases dropwindsondes around tropical cyclones in the North Atlantic and central and eastern North Pacific basins (Dorst 2007). The G-IV dropwindsondes supply environmental information for forecasters and operational data assimilation systems to create short-term forecast improvements (Aberson and Franklin 1999; Ryan et al. 2019). During the period for TC PRIMED from 1998 to 2019, the G-IV collected data from nearly 12 000 dropwindsondes via the NCAR Airborne Vertical Atmospheric Profiling System (AVAPS) dropwindsonde system (Hock and Franklin 1999). The dropwindsondes in the AVAPS D-file output format from the G-IV are available from the NOAA Atlantic Oceanographic and Meteorological Laboratory Hurricane Research Division database. During this period, the G-IV has used the RD93, RD94, and RD41 research dropwindsondes with GPS navigation system for wind. As dropwindsonde technology, analysis, and research continue to evolve, researchers have found biases in some instruments. For example, RD94 from 2008 onward

exhibit a dry bias (Vömel et al. 2016). The developers have implemented corrections for these biases in the Atmospheric Sounding Processing Environment (ASPEN) software that allows for reprocessing of the existing AVAPS D-file data. Here, we reprocess all G-IV dropwindsondes from 1998 to 2019 with ASPEN version 3.4.6 released on 1 May 2021. We opt for the default quality control constraints because the G-IV synoptic surveillance dropwindsondes do not encounter extremes to warrant changing the constraints, as done by Stern et al. (2016) for analysis of the inner-core area of the storm. And, we do not take other post-mission quality control steps such as those outlined by Ciesielski et al. (2012).

3. Large-scale environment

The tropical cyclone environment plays a substantial role in storm development and evolution. With respect to the operational representation of the environment as scalar quantities, diagnostic algorithms calculate multiple storm-centered averages to capture the area that exhibits the greatest influence on tropical cyclones, in Fig. 1. To generate the storm-centered representation of the environment, we locate the storm position within the model fields, interpolate the model fields to a polar grid, calculate quantity-specific area averages, and compute additional derived metrics.

a. Storm position

Models do not always place tropical cyclones in the same location as the best-track database positions. The displacement error is related to the uncertainties in the best-track position (Torn and Snyder 2012; Landsea and Franklin 2013; Combot et al. 2020) and issues with resolving the vortex (Davis 2018). Resolving the tropical cyclone is problematic for many reanalysis products (Hodges et al. 2017) in that the reanalysis is run at a coarse resolution compared to the forecast version of the model. Whether for a forecast or a reanalysis, the modeled tropical cyclone center needs to be located with a vortex tracker algorithm.

For the Global Forecast System and other NCEP models, the NOAA Geophysical Fluid Dynamics Laboratory (GFDL) vortex tracker (Marchok 2002, 2021) runs to supply track, intensity, and wind radii information. However, the ERA5 product does not provide tropical cyclone vortex tracker output. Vortex trackers vary in complexity, but follow the GFDL vortex tracker steps (Marchok 2002, 2021). For an existing vortex, a position or fix from an outside source or previous forecast acts as the first guess. Then, the tracker extracts a subset of the model output fields (e.g., low-level fields for tropical cyclones) to use with an optimization routine. Because model output is often not on the native model grid and the vortex center may be subgrid scale, the vortex center finding procedure requires interpolation to capture the center. For this step, the GFDL vortex tracker uses multiple iterations of a single-pass Barnes analysis (Barnes 1964) to detect the subgrid-scale center and to regularize the procedure across multiple model grid types and resolutions. Since the center position varies across fields, the tracker averages the positions to create the final model vortex position. In the

1998 configuration, the GFDL vortex tracker used 700- and 850-hPa relative vorticity, geopotential height, and wind speed along with mean sea level pressure.

Here, we use the final best-track position from the ATCF as our initial guess for the location of the tropical cyclone vortex. Then, we subset a selection of reanalysis product output fields on a 4° × 4° domain. Marchok (2021) shows that 850-hPa geopotential height is the best single field, and that including other near-surface parameters improves the tracker performance to be close to a more complex version with 11 different model fields. Additionally, Marchok (2021) finds that a simple parameter configuration with 850-hPa geopotential height and mean sea level pressure is sufficient when not following a vortex in the forecast fields. Since we restart the center finding for each analysis and do not follow the vortex, we choose this simple parameter configuration. Because we are limiting this work to a single model with a consistent resolution, we do not use the single-pass Barnes analysis. Instead, we use a bivariate cubic spline and a limited-memory Broyden–Fletcher–Goldfarb–Shanno optimization algorithm (Byrd et al. 1995) to find the position of the local extrema within our 4° × 4° domain. Then, we average the positions of the vortex center to create our final estimate of the center position.

Using the final best-track position and center position located in ERA5, we calculate the position offset. Figure 2 shows probability density function diagrams of the position offsets for intensities (a) between 34 and 63 kt, (b) between 64 and 95 kt, and (c) greater than 95 kt in 10-km bins. The black curve (labeled "All") shows the offset for global tropical cyclones, with the overall median offset being near 25 km—note that an approximate resolution of ERA5 is 31 km. Hodges et al. (2017) show that many reanalysis products prior to ERA5 have a median displacement between 50 and 100 km. Figures 2a–c also include the distribution of center displacements for North Atlantic (AL; green curve), eastern North Pacific (EP; purple curve), western North Pacific (WP; blue curve), north Indian Ocean (IO; orange curve), and Southern Hemisphere (SH; red curve) basins. From these panels, the North Atlantic appears to have the smallest center offsets, which is likely attributable to routine reconnaissance data in the western portion of the basin. The Southern Hemisphere exhibits the largest position offsets, which can likely be attributed to fewer observations in comparison to the Northern Hemisphere and best-track information not being used in the ERA5 data assimilation system. The time series of the seasonal mean offset from 1998 to 2019 (Fig. 2d) [shown for all intensities (black curve) and for intensities between 34 and 63 kt (dark blue curve), between 64 and 95 kt (dark purple curve), and greater than 95 kt (dark green curve) with the one standard deviation (light curves)] shows a decrease in the mean offset over time from roughly 75 to 50 km and a decrease in the offset standard deviation from roughly 50 to 25 km. We believe that this is due to the increase of observations available for data assimilation. In comparison to the reanalysis products evaluated by Hodges et al. (2017), ERA5 has smaller displacement error compared to the best-track database.
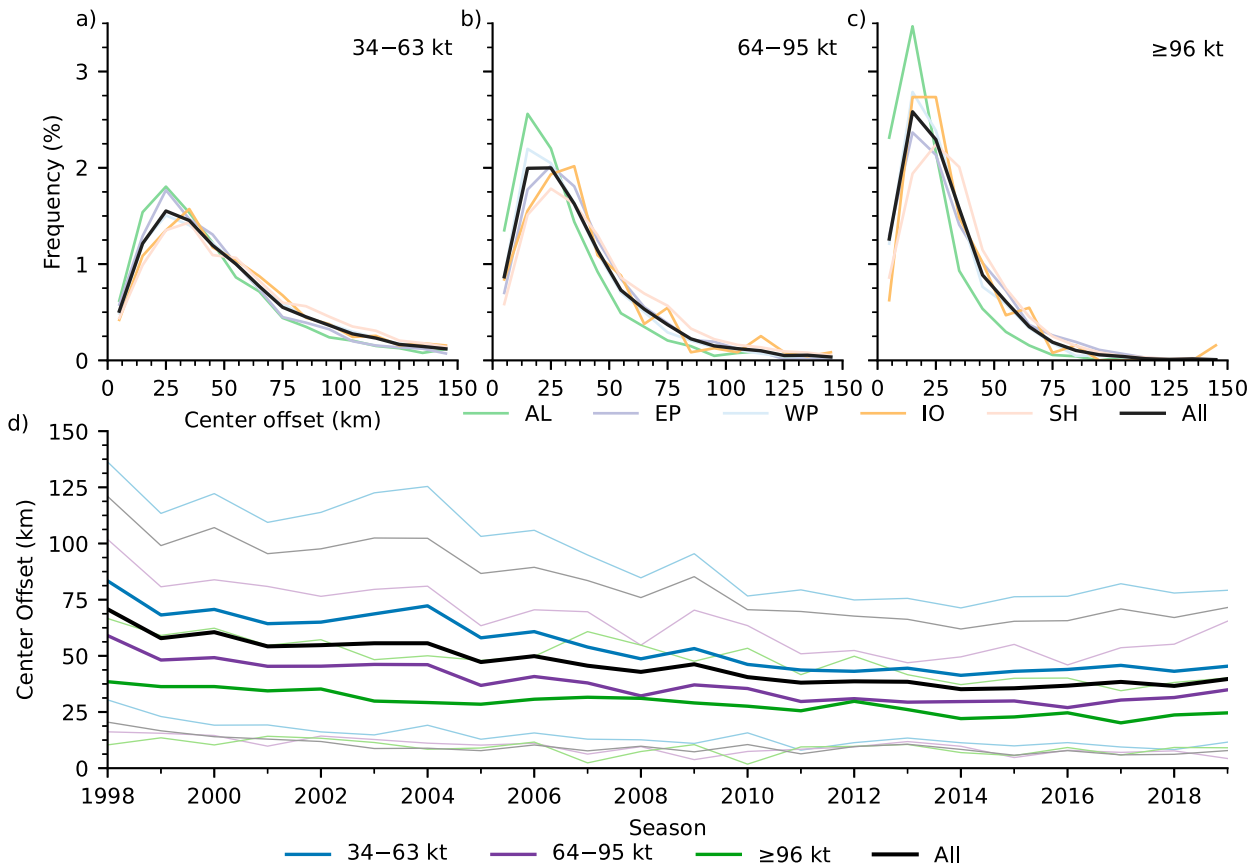
FIG. 2. Tropical cyclone position offset between the final best-track position and the center in ERA5 for intensities (a) between 34 and 63 kt, (b) between 64 and 95 kt, and (c) greater than 95 kt in normalized 10-km bins for global (All; black curve), the North Atlantic (AL; green curve), eastern North Pacific (EP; purple curve), western North Pacific (WP; blue curve), north Indian Ocean (IO; orange curve), and Southern Hemisphere (SH; red curve) tropical cyclones. (d) The offset from 1998 to 2019 for all intensities (black curve) and intensities between 34 and 63 kt (dark blue curve), between 64 and 95 kt (dark purple curve), and greater than 95 kt (dark green curve) with plus or minus one standard deviation (light curves).

b. Area averaging and metrics

To calculate the tropical cyclone environmental quantities in SHIPS operational large-scale diagnostics and the SHIPS developmental dataset, the large-scale diagnostic algorithm crudely removes the tropical cyclone vortex by subtracting the area-averaged wind field. However, this vortex removal process does not remove the associated thermodynamic fields [for a dynamical approach, see Winterbottom and Chassignet (2011)]. By removing the vortex, SHIPS can calculate diagnostic quantities along the official forecast track or best-track vortex position. An alternative is to calculate so-called model diagnostics at the model vortex position (McNoldy et al. 2010)—the approach taken here. While the model diagnostic approach does not explicitly remove the vortex, the area averaging does eliminate the symmetric component of the wind field.

Using the model storm center, our next step is to take an area average of the rectilinear field (first column in Fig. 3 for Hurricane Harvey at 0000 UTC 26 August 2017 for relative humidity, temperature anomaly relative to 1500 km from the

center, and wind). Following the approach used in calculating the SHIPS large-scale diagnostics, we use bilinear interpolation to map the 0.25° × 0.25° ERA5 product output onto a 5-km radius × 5° azimuth polar grid out to 1500 km from the model storm center position (shown for Hurricane Harvey in the second column in Fig. 3 out to 1000 km in radius). Next, we calculate area averages of the wind, temperature, relative humidity, geopotential height, divergence, and vorticity. In the SHIPS developmental dataset (DeMaria et al. 2005), the diagnostic algorithm calculates quantities over multiple radial ranges, but only outputs a subset of pressure levels. SHIPS model diagnostics (McNoldy et al. 2010) stay with a prespecified area-average for a specific state variable. Here, we create profiles that are area averaged from 0 to 1000 km at every pressure level for divergence and relative vorticity. For the kinematic and thermodynamic fields (i.e., temperature, relative humidity, geopotential height, and wind), we create vertical profiles with an area average from 0 to 500 km and from 200 to 800 km. Table 1 provides a summary of averaging areas. Figures 3g and 3h show the 200–800-km area-averaged temperature and dewpoint temperature calculated from the
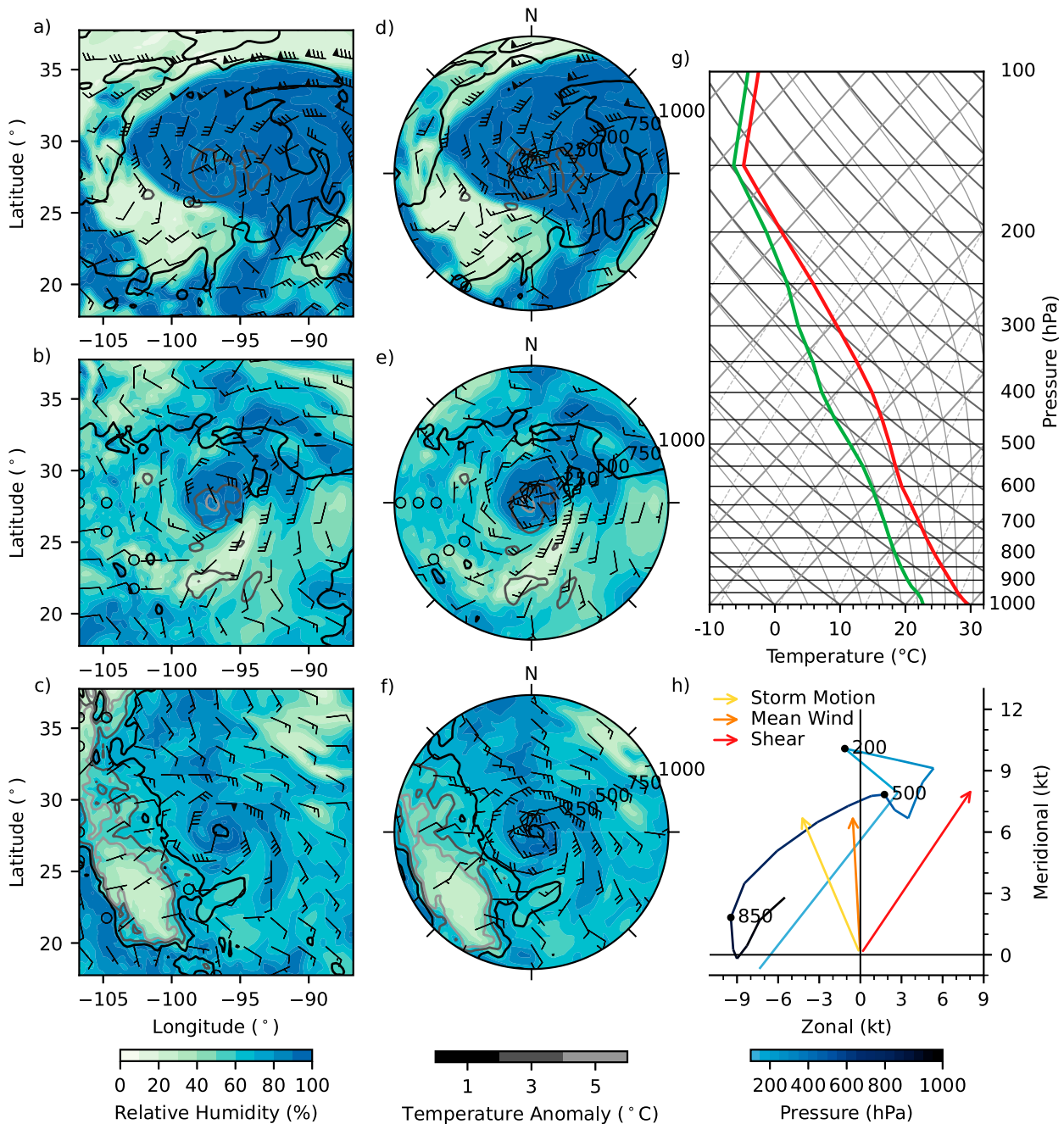
FIG. 3. (a)–(c) Relative humidity (green to blue shading at 10% intervals), temperature anomaly calculated from the 1500-km mean profile (grayscale contours at 1°C intervals), and wind (barbs; in kt) in a 20° × 20° domain on the 0.25° ERA5 grid centered on Hurricane Harvey at 0000 UTC 26 Aug 2017 for 200, 500, and 850 hPa, respectively. (d)–(f) As in (a)–(c), but out to 1000 km from the storm center for (d) 200, (e) 500, and (f) 850 hPa after bilinear interpolation to a 5 km in radius and 5° in azimuth cylindrical grid. (g) The skew T–log$p$ diagram depicts the 200–800-km temperature (red curve) and dewpoint temperature (green curve). (h) A hodograph shows the 0–500-km wind (shaded in dark blue to light blue as a function of pressure) with 200, 500, and 850 hPa labeled and storm motion vector (yellow arrow), 200–850-hPa mean wind vector (orange arrow) used for the generalized shear, and the deep-layer shear vector (red arrow).

relative humidity on a skew T–log$p$ diagram and 0–500-km wind on a hodograph as an example of these vertical profiles.

The SHIPS-based diagnostics include two forms of vertical wind shear: generalized and layered. Deep-layer vertical wind

shear is an example of layered shear and is the difference between the 200- and 850-hPa wind vectors, and we define it as

$$V_{mag} = [(u_{200} - u_{850})^2 + (v_{200} - v_{850})^2]^{1/2}, \qquad (1)$$

where u_p and v_p are the zonal and the meridional components of the wind at $p = 200, 850$ hPa. We calculate the direction of V_{mag} with

$$V_{dir} = \cos^{-1}\left(\frac{u_{200} - u_{850}}{V_{mag}}\right) + \begin{cases} \dfrac{\pi}{2} & \text{if } (v_{200} - v_{850}) < 0, \\ 0 & \text{otherwise,} \end{cases} \quad (2)$$

where V_{dir} is in radians and then converted to standard meteorological heading. We do not calculate other layer shear quantities—the wind profile data in the TC PRIMED environmental file allow for easy calculation of other shear metrics. The layer shear quantities miss wind profile variability that may come from strong winds concentrated in a shallow layer aloft or middle-tropospheric shear (Elsberry and Jeffries 1996; Velden and Sears 2014). To address this deficiency, Knaff et al. (2005) define the second form of shear included in the SHIPS large-scale diagnostics called generalized shear that removes the column mean wind profile and computes the mass-weighted sum of the remainder. From Knaff et al. (2005), the generalized shear is

$$\mathcal{G} = 4\sum_{i=1}^{I} w_p[(u_p - \overline{u})^2 + (v_p - \overline{v})^2]^{1/2}, \quad (3)$$

where i is the pressure level index for pressure values p from 850 to 200 hPa, I is the total number of pressure levels, w is the mass weight for the pressure level p, and $\overline{u}$ and $\overline{v}$ are the column-averaged zonal and meridional wind. The SHIPS algorithm calculates the shear from 0 to 500 km, the value used operationally, and from 200 to 800 km. We also calculate the deep-layer and generalized wind shear with the 200–800-km zonal and meridional wind profiles and those values are available in TC PRIMED. For the 0–500-km calculations, Fig. 3h shows the wind profile (blue curve), the deep-layer shear vector as a red arrow, the 200–850-hPa mean wind vector used in the generalized shear as an orange arrow, and the storm motion vector as a yellow arrow for reference.

Here, we compute the temperature gradient and advection from the geostrophic thermal wind equation as

$$\text{TADV} = -\overline{u}\,\frac{\partial T}{\partial x} - \overline{v}\,\frac{\partial T}{\partial y} \quad \text{and} \quad (4)$$

$$\text{TGRD} = \left[\left(\frac{\partial T}{\partial x}\right)^2 + \left(\frac{\partial T}{\partial y}\right)^2\right]^{1/2}, \quad (5)$$

where $\overline{u}$ and $\overline{v}$ are the average 700- and 850-hPa winds and

$$\frac{\partial T}{\partial x} = -\frac{f}{R_0}\,\frac{\partial u}{\partial \ln p} \quad \text{and} \quad (6)$$

$$\frac{\partial T}{\partial y} = -\frac{f}{R_0}\,\frac{\partial v}{\partial \ln p}, \quad (7)$$

where f is the Coriolis parameter as a function of storm center latitude and R_0 is the gas constant. To vertically discretize, we estimate $\partial \ln p$ as $\ln(p_{850}/p_{700})$ and ∂u and ∂v as the differences between the 700- and 850-hPa winds.

In addition to temperature gradient and advection, we calculate an azimuthal mean environmental temperature profile at a radius of 1500 km chosen based on Frank (1977) and a temperature anomaly defined as the temperature profile area-averaged from 0 to 15 km minus the azimuthal-mean environmental temperature profile (shown for a larger area in the left and middle columns of Fig. 3 to provide an example of temperature anomaly). Because our focus is on the storm environment, we will not offer further discussion of the temperature anomaly profile except to note that the ERA5 eye temperature anomaly will be smaller than the anomaly of the storm because this cannot be resolved; Davis (2018) discusses the impact of model resolution on the intensity and radius of maximum wind.

To assess a measure of convective instability, we use the temperature and moisture environmental profiles. Since measures such as convective available potential energy do not work in the tropics (Zipser 2003), we compute a density-weighted convective mass flux from DeMaria (2009). DeMaria (2009) uses an entraining plume model after Simpson and Wiggert (1969) combined with the thermodynamics and bulk microphysics of Ooyama (1990) to include the water and ice phase condensate weight. As a summary of this and the other area-averaged variables and derived metrics discussed in this section, we provide brief descriptions in Table 1 and detailed descriptions in Tables S1–S4 in the online supplemental material.

c. Storm position and shear metric error

An erroneous tropical cyclone center selection in the reanalysis fields will result in errors in the large-scale environmental quantities. For most quantities, this effect will be small (e.g., temperature fields in the tropics). However, the vertical wind shear metric calculation assumes that our approach identifies a correct storm center position and that this center position represents the storm at all vertical levels. Position locating issues or a lack of vertical alignment might result in erroneously high values because the azimuthal averaging would not completely remove the symmetric component of the wind field and some storm-induced shear would remain in the azimuthal average.

To estimate the errors in the wind shear quantities, we reprocess the ERA5 product fields by adding a random perturbation to the tropical cyclone center position. To perturb the center, we sample from a Gaussian distribution with a standard deviation of 50 km, which is the forecaster estimate of best-track position error for satellite-only center fixing in the North Atlantic (Landsea and Franklin 2013). With this approach over the TC PRIMED period from 1998 to 2019, the mean absolute deviation is 1.3 and 0.8 kt and the standard deviation is 0.8 and 0.5 kt for the 0–500- and 200–800-km deep-layer vertical wind shear, respectively. The mean absolute deviation for the 0–500- and 200–800-km vertical wind shear is 8.2% and 4.7% of the mean shear values, 15.9 and 17.1 kt respectively, in the ERA5 diagnostic quantities. Figure 4 shows (a) the distribution of the randomly generated position offsets between the centers used for calculating the
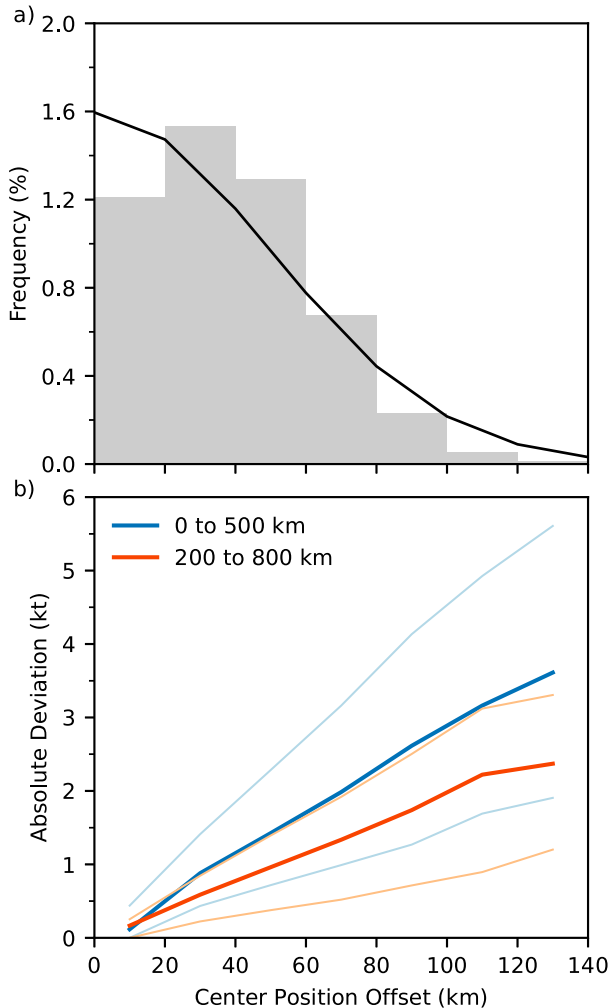
FIG. 4. (a) The center position offset from the centering finding technique and random perturbations as a function of radius (gray bars) and a Gaussian distribution (black curve) with a 50-km standard deviation. (b) The median absolute deviations (dark curves) and the 25th and 75th percentiles (light curves) between the deep-layer vertical wind shear calculated between the two centers for the 0–500-km (blue curves) and 200–800-km (orange curves) azimuthal averages.

diagnostic quantities from ERA5 for TC PRIMED in gray bars overlaid with the Gaussian distribution in the black curve and the perturbed centers and the 25th and 75th percentiles and median deviation for the (b) 0–500-km (blue curves) and 200–800-km (orange curves) deep-layer vertical wind shear as a function of offset distance. The relatively small deviations in the vertical wind shear metrics are likely a result of model resolution being approximately 31 km and interpolated to a 0.25° output grid. The sensitivity to the position offset in mesoscale models is likely larger and should be evaluated before assuming that the result for ERA5 applies more broadly.

As a note for applications using TC PRIMED when a center might naturally be ill defined such as during extratropical

transition or for tropical storms and depressions, the operational SHIPS algorithm switches from the 0–500-km to the 200–800-km deep-layer vertical wind shear quantity when the storm position is unknown as a strategy for mitigating center position issues. As shown by Fig. 4, position-offset-related deviations are smaller for the 200–800-km vertical wind shear.

4. ERA5 and SHIPS

In contextualizing the tropical cyclone environment for the National Hurricane Center, Central Pacific Hurricane Center, and Joint Typhoon Warning Center statistical–dynamical guidance, the tropical cyclone research community often leverages the SHIPS large-scale diagnostic quantities. In TC PRIMED, we calculate the model diagnostics from the ERA5 products to provide more metrics for tropical cyclone applications from a single source. With the SHIPS developmental dataset being the tropical cyclone research communities' main source of environmental data, we compare the diagnostics calculated from over 47 300 synoptic periods to estimate uncertainty.

To quantify the differences between the two sets of diagnostics, we focus on the thermodynamic and kinematic profiles and calculate the median and the 25th and 75th percentiles for the quantities and differences. For kinematic quantities, Fig. 5 shows these comparisons of ERA5 (dark bars) with SHIPS (light bars) for all (gray) and individual basins [North Atlantic (AL), green; eastern North Pacific (EP), purple; western North Pacific (WP), blue; north Indian Ocean (IO), orange; Southern Hemisphere (SH), red] for the 1998–2019 seasons. Figures 5a and 5b show values and differences for the 200–850-hPa deep-layer vertical wind shear (SHDC), generalized wind shear (SHGC), and 0–500-km 200-hPa zonal (U20C) and meridional (V20C) wind. The interquartile range for deep-layer shear (SHDC) from both datasets is 9–21 kt with a bias for ERA5 relative to SHIPS between 0.0 and 0.5 kt. The uncertainty of the layered vertical wind shear in ERA5 caused by the center position is within this uncertainty range. Generalized shear (SHGC) has more variability with a range from 17 to 36 kt. ERA5 shows a 1.0–1.5-kt bias compared to SHIPS. Meridional and zonal winds range from −15 to 15 kt with small biases. For the vertical wind shear metrics, the North Atlantic shows the smallest range in variations between SHIPS and ERA5, and the Southern Hemisphere exhibits the largest variations.

For thermodynamic quantities, Figs. 5c and 5d show the values and differences for the following 200–800-km relative humidity (%) diagnostics: 1000 hPa (R000), 700–850 hPa (RHLO), 500–700 hPa (RHMD), and 300–500 hPa (RHHI). ERA5 shows a 5% moisture bias at 1000 hPa with values ranging from 75% to 85% while SHIPS is drier with values ranging from 68% to 80%. This signal reverses for the 700–850-, 500–700-, and 300–500-hPa layered relative humidity quantities with ERA5 being 2% drier than the SHIPS developmental dataset. Figures 5e and 5f show the temperature, with Fig. 5e presented as an anomaly relative to the North Atlantic July–October mean atmosphere (Dunion 2011) with values of 26.4°, 43.3°, 55.2°, and 67.6°C for 1000, 250, 200, and 150 hPa, respectively. Overall, temperature shows a small
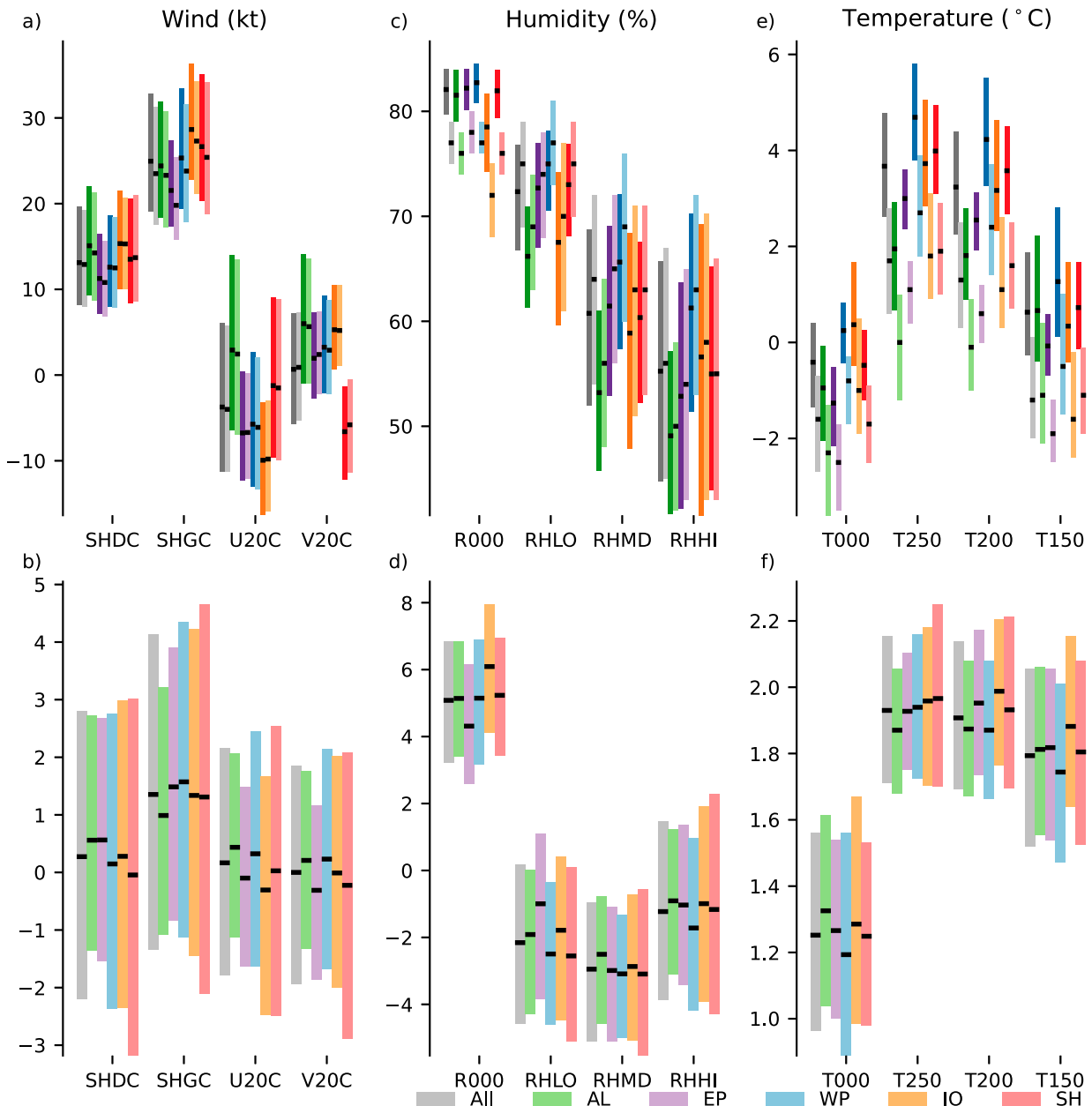
FIG. 5. A comparison between ERA5 (dark bars) and SHIPS (light bars) diagnostics for all (gray bar) and individual basins [North Atlantic (AL), green; eastern North Pacific (EP), purple; western North Pacific (WP), blue; north Indian Ocean (IO), orange; Southern Hemisphere (SH), red] from the 1998–2019 season, showing (top) the median and the 25th and 75th percentiles of diagnostic quantities and (bottom) the difference between ERA5 and SHIPS. (left) 0–500-km wind-based (kt) diagnostics: deep-layer (SHDC) and generalized (SHGC) wind shear and 200-hPa zonal (U20C) and meridional (V20C) wind. (center) 200–800-km relative humidity (%) diagnostics: 1000 hPa (R000), 700–850 hPa (RHLO), 500–700 hPa (RHMD), and 300–500 (RHHI). (right) 200–800-km temperature (°C) diagnostics: 1000 hPa (T000), 250 hPa (T250), 200 hPa (T200), and 150 hPa (T150). Note that (e) is offset with the mean sounding in Dunion (2011) using the values of 26.4°, 43.3°, 55.2°, and 67.6°C for 1000, 250, 200, and 150 hPa, respectively.

range of 1°–2°C. For the 1000-, 250-, 200-, and 150-hPa 200- to 800-km temperature, ERA5 has a warm bias with a median bias of 1.2°C at 1000 hPa and near 1.9°C at 250, 200, and 150 hPa. Table 2 provides this uncertainty information from the differences between ERA5 and SHIPS. Through performing a

paired-difference Student's t test, we reject the null hypothesis that the mean differences are zero at the statistical significance level of $\alpha = 0.01$ for all metrics except the 200–850-hPa deep-layered vertical wind shear (SHDC). For SHDC, we fail to reject the null hypothesis.

TABLE 2. The mean μ and standard deviation σ of the bias in the second and third columns. The quantity sample standard deviation provides scaled versions of these values in parentheses. The remaining columns provide the 25th, 50th (median), and 75th percentiles in the fourth, fifth, and sixth columns, and the μ and σ of ERA5 (roman) and SHIPS (italics). The quantity identifiers in the first column represent the 200–850-hPa deep-layer vertical wind shear (SHDC), generalized wind shear (SHGC), and 0–500-km 200-hPa zonal (U20C) and meridional (V20C) wind, 200–800-km relative humidity (%) diagnostics for 1000 hPa (R000), 700–850 hPa (RHLO), and 500–700 hPa (RHMD), 300–500 (RHHI), as well as the 200–800-km temperature (°C) diagnostics: 1000 hPa (T000), 250 hPa (T250), 200 hPa (T200), and 150 hPa (T150). Note that for all metrics except SHDC, a paired-difference Student's t test yields a rejected null hypothesis at a significance level of $\alpha = 0.01$.

	Bias		Percentile				
Quantity	μ	σ	25th	50th	75th	μ	σ
SHDC (kt)	0.02 (0.09)	5.59 (0.56)	8.2	13.1	19.6	14.9	9.4
			8.0	*12.9*	*19.3*	*14.9*	*10.0*
SHGC (kt)	1.17 (0.26)	6.02 (0.52)	19.1	25.0	32.0	27.1	11.0
			17.7	*23.5*	*31.3*	*25.9*	*11.8*
U20C (kt)	0.12 (0.01)	4.74 (0.33)	−11.3	−3.7	6.1	−1.4	14.2
			−11.3	*−4.0*	*5.7*	*−1.6*	*14.4*
V20C (kt)	−0.22 (−0.02)	4.80 (0.43)	−5.7	0.7	7.2	1.1	11.3
			−5.3	*0.9*	*7.3*	*1.3*	*11.1*
R000 (%)	5.09 (2.02)	3.04 (0.68)	79.7	82.1	84.1	81.4	4.4
			75.0	*77.0*	*79.0*	*76.3*	*4.6*
RHLO (%)	−2.05 (0.38)	4.30 (0.55)	66.7	72.3	76.8	71.2	7.4
			69.0	*74.0*	*79.0*	*73.2*	*8.0*
RHMD (%)	−2.68 (0.19)	5.16 (0.42)	51.8	60.7	68.7	60.0	11.6
			54.0	*64.0*	*72.0*	*62.5*	*12.6*
RHHI (%)	−0.78 (0.19)	6.00 (0.39)	44.7	55.2	65.7	54.9	14.3
			45.0	*56.0*	*67.0*	*55.7*	*15.2*
T000 (°C)	1.28 (0.67)	0.54 (0.30)	25.1	26.0	26.8	25.8	1.7
			23.7	*24.8*	*25.7*	*24.6*	*1.8*
T250 (°C)	1.97 (0.99)	0.53 (0.27)	−40.7	−39.6	−38.5	−39.7	2.0
			−42.7	*−41.6*	*−40.5*	*−41.6*	*2.0*
T200 (°C)	1.92 (1.09)	1.77 (0.27)	−53.0	−52.0	−50.8	−51.8	1.8
			−54.9	*−53.9*	*−52.7*	*−53.8*	*1.8*
T150 (°C)	0.99 (1.00)	1.79 (0.27)	−67.9	−67.0	−65.7	−66.6	1.8
			−69.6	*−68.8*	*−67.7*	*−68.4*	*1.8*

To provide season-to-season variability, Fig. 6 shows the same quantities now presented as a seasonal time series without the basin perspective and the mean and standard deviation rather than the median and the 25th and 75th percentiles. For all quantities, the same general pattern applies in that the mean deviation between ERA5 and SHIPS remains fairly stable over time, but the standard deviation decreases slightly. The most notable change in time is in low-level relative humidity with ERA5 becoming moister in time and having no bias relative to SHIPS by 2010. We expect systematic biases in the SHIPS developmental dataset due to using both CFSR and the operational version of the GFS, which will contain inconsistencies due to routine operational model updates. However, the relative stability of the mean differences across the diagnostic quantities suggests that the definitions are relatively robust to subtle changes or that the models resolve these quantities at these scales. The variability in the standard deviation could be a result of systematic biases or interannual variability.

For the derived metrics, we assess generalized vertical wind shear [Eq. (3), as shown in the last section], convective mass flux from the entrained plume model with ice and liquid phases and 700–850-hPa temperature advection [Eq. (4)] and gradient [Eq. (5)] from the geostrophic thermal wind equation.

We compare the derived diagnostic metrics because these tend to enhance subtle differences across multiple layers in the vertical profile. Figure 7 shows probability density function plots of the four metrics for the individual basins with least squares regression lines for the North Atlantic (AL, green), eastern North Pacific (EP, purple), western North Pacific (WP, blue), north Indian Ocean (IO, orange), and Southern Hemisphere (SH, red). The SHIPS and ERA5 generalized shear values (Fig. 7a) are highly correlated with little spread. However, the deviations in shear between ERA5 and SHIPS are larger for low and high shear values in the Southern Hemisphere basin than in the Northern Hemisphere tropical cyclone basins. The convective mass flux calculated using the 200–800-km-averaged temperature and relative humidity shows that ERA5 has less convective instability than SHIPS. The temperature gradient and advection (Figs. 7c and 7d) show that the two quantities are in relative agreement between the two models, but suggest that the low-level winds have higher variability than the 200-hPa wind component as shown in Fig. 5a.

5. Comparison to observations

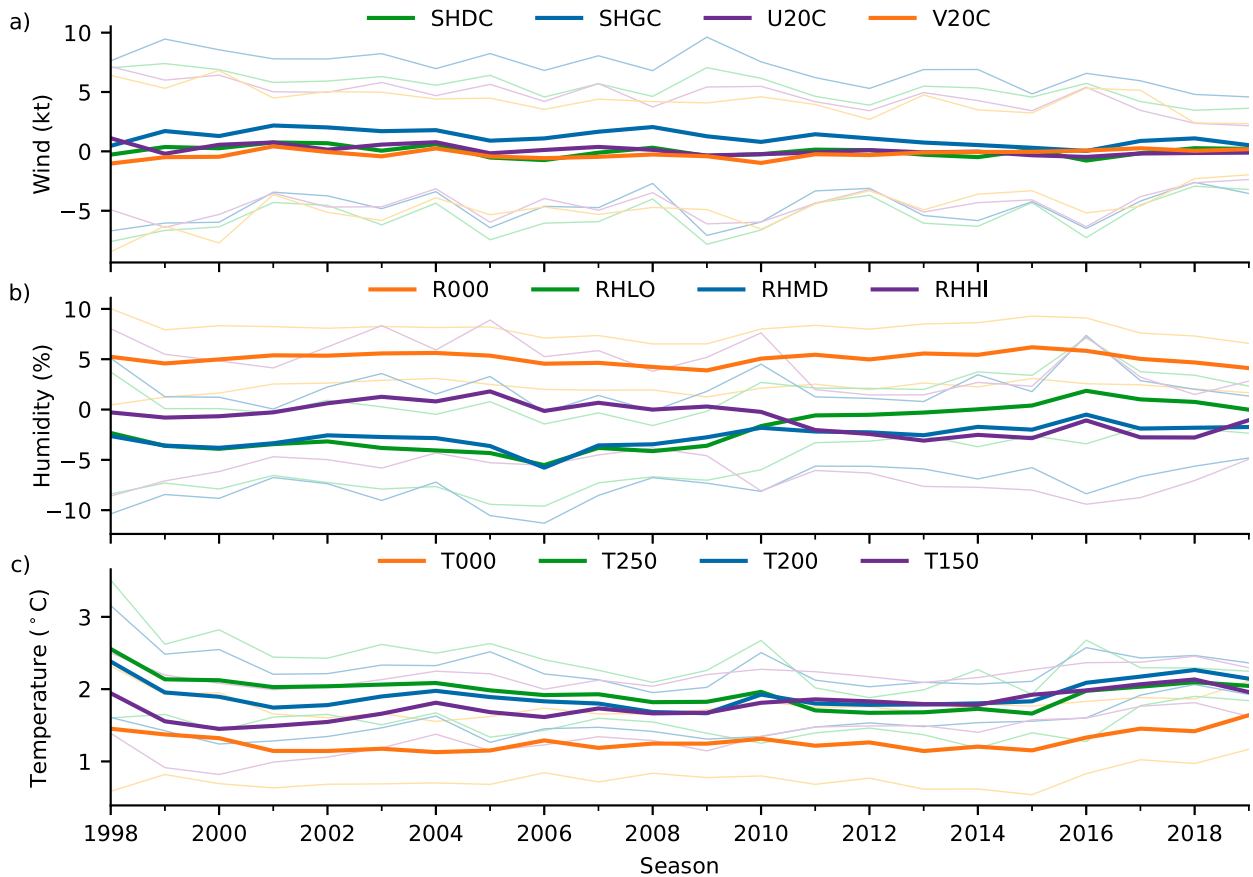Comparing two versions of diagnostics quantities does not provide context for how well the metrics or model represent

FIG. 6. Time series showing the mean (thick curve) and ±one standard deviation (thin curves) of the differences between ERA5 diagnostics and the SHIPS developmental dataset from the 1998–2019 season. (a) Wind-based (kt) diagnostics: 200–850-hPa deep-layer vertical wind shear (SHDC; green), generalized wind shear (SHGC; blue), and 0–500-km 200-hPa zonal (U20C; purple) and meridional (V20C; orange) wind. (b) 200–800-km relative humidity (%) diagnostics for 1000 hPa (R000; orange), 700–850 hPa (RHLO; green), 500–700 hPa (RHMD; blue), and 300–500 (RHHI; purple). (c) 200–800-km temperature (°C) diagnostics for 1000 hPa (T000; orange), 250 hPa (T250; green), 200 hPa (T200; blue), and 150 hPa (T150; purple).

and resolve observed tropical cyclones. To understand the synoptic-scale representation of ERA5, we provide uncertainty for the model fields to the kinematic and thermodynamic diagnostic quantities to dropwindsondes.

To understand the kinematic and thermodynamic representation of the tropical cyclone environment in ERA5, we use G-IV dropwindsonde data. Because dropwindsondes have more degrees of freedom than ERA5 in sampling the atmosphere at 2 Hz and do not represent a large-scale quantity, we process both datasets to create a realistic comparison that offers insight into any potential systematic biases in ERA5 and capture the spread or uncertainty in diagnostic quantities. To do this, we apply a vertical smoothing to the dropwindsondes to be more indicative of the vertical resolution of the ERA5 pressure-level product, conduct a storm-relative analysis by interpolating ERA5 to the storm-relative radius and azimuth of the dropwindsonde launch, and area-average profiles and diagnostic quantities for flights where dropwindsondes encircle a storm.

To create an ERA5–dropwindsonde composite analysis, we smooth the dropwindsonde observations in the vertical with a

Gaussian weighted-averaging technique [i.e., the first pass in the analysis in Barnes (1964)]. We calculate the Gaussian weighted average with

$$g_k = \frac{\sum_{m=1}^{M} w_m f_m}{\sum_{m=1}^{M} w_m},$$ (8)

where k is a grid point representing a fixed pressure surface, p, ranging from 100 to 1000 hPa at 50-hPa intervals with the addition of 925 and 975 hPa, g is the value of the Gaussian weighted average at k, m is a dropwindsonde measurement, M is the total number of dropwindsonde measurements, f is the observed state variable at m, and w is the weight assigned to m as a known function of vertical displacement, r_m. Here, we define the vertical displacement of the measurement m and the grid point k in terms of the pressure p. We define the weights as
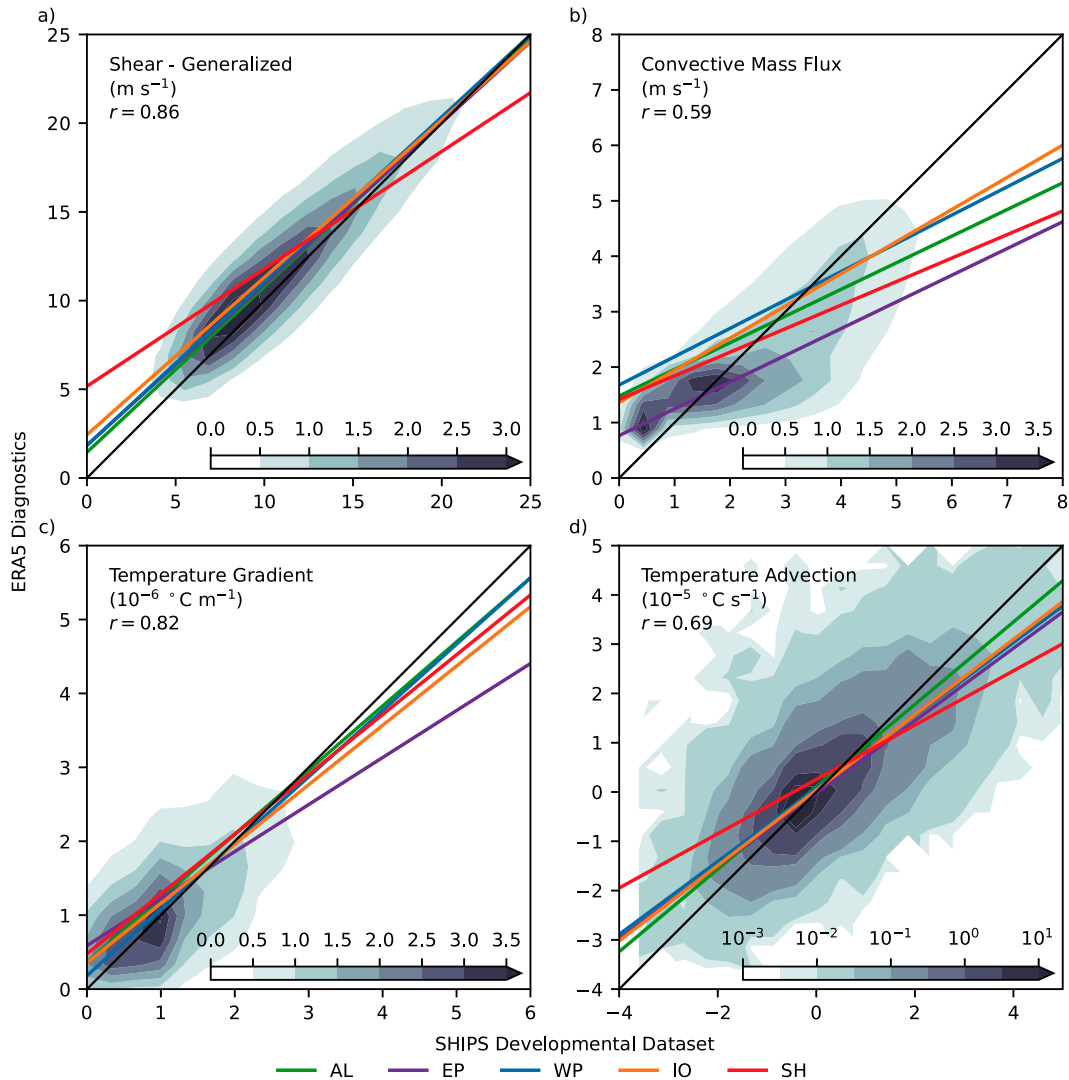
FIG. 7. Probability distribution (frequency shaded) of diagnostic metrics calculated from the area-averaged SHIPS developmental dataset (abscissa) and ERA5 (ordinate) for (a) 0–500-km generalized wind shear, (b) 200–800-km convective mass flux calculated from temperature and relative humidity with an entrained plume model, (c) 0–500-km 700–850-hPa temperature gradient, and (d) 0–500-km 700–850-hPa temperature advection. Each panel shows the least squares regression for the North Atlantic (AL; green curve), eastern North Pacific (EP; purple curve), western North Pacific (WP; blue curve), north Indian Ocean (IO; orange curve), and Southern Hemisphere (SH; red curve). Each panel shows the one-to-one line (thin black curve) and r, the Pearson correlation coefficient for all basins.

$$w_m = \begin{cases} \exp\left(-\dfrac{r_m^2}{r_e^2}\right) & \text{if } r \leq r_c, \\ 0 & \text{if } r > r_c, \end{cases} \tag{9}$$

where r_e is the e-folding displacement and r_c is the critical value of the displacement in which a measurement influences the weighted average. We approximate the critical value as $r_c \approx \sqrt{20r_e^2}$, which is where $w_m = 2 \times 10^{-9}$. Here, we select $r_e = 2.5$ hPa, which means that $r_c \approx 11$ hPa.

After processing, we interpolate the ERA5 product fields to the radius and azimuth location and time of the dropwindsonde

launch. While ERA5 output is available hourly, we only use the synoptic hour analyses from TC PRIMED. We take the fields from the two nearest synoptic times and apply weighting using

$$f(t) = f_1(t_1)S\left(\frac{t - t_1}{\Delta t}\right) + f_2(t_2)S\left(\frac{t_2 - t}{\Delta t}\right), \tag{10}$$

where $t_1 \leq t \leq t_2$, $\Delta t = t_2 - t_1 = 6$ h, $S(s) = 1 - 3s^2 + 2s^3$ is the basic cubic Hermite shape function that satisfies $S(0) = 1$ and $S(1) = 0$ as well as $S'(0) = S'(1) = 0$, and $f_1(t_1)$ and $f_2(t_2)$ are the values of the ERA5 field at the specific location for times t_1 and t_2, respectively. For a location in space for the fields
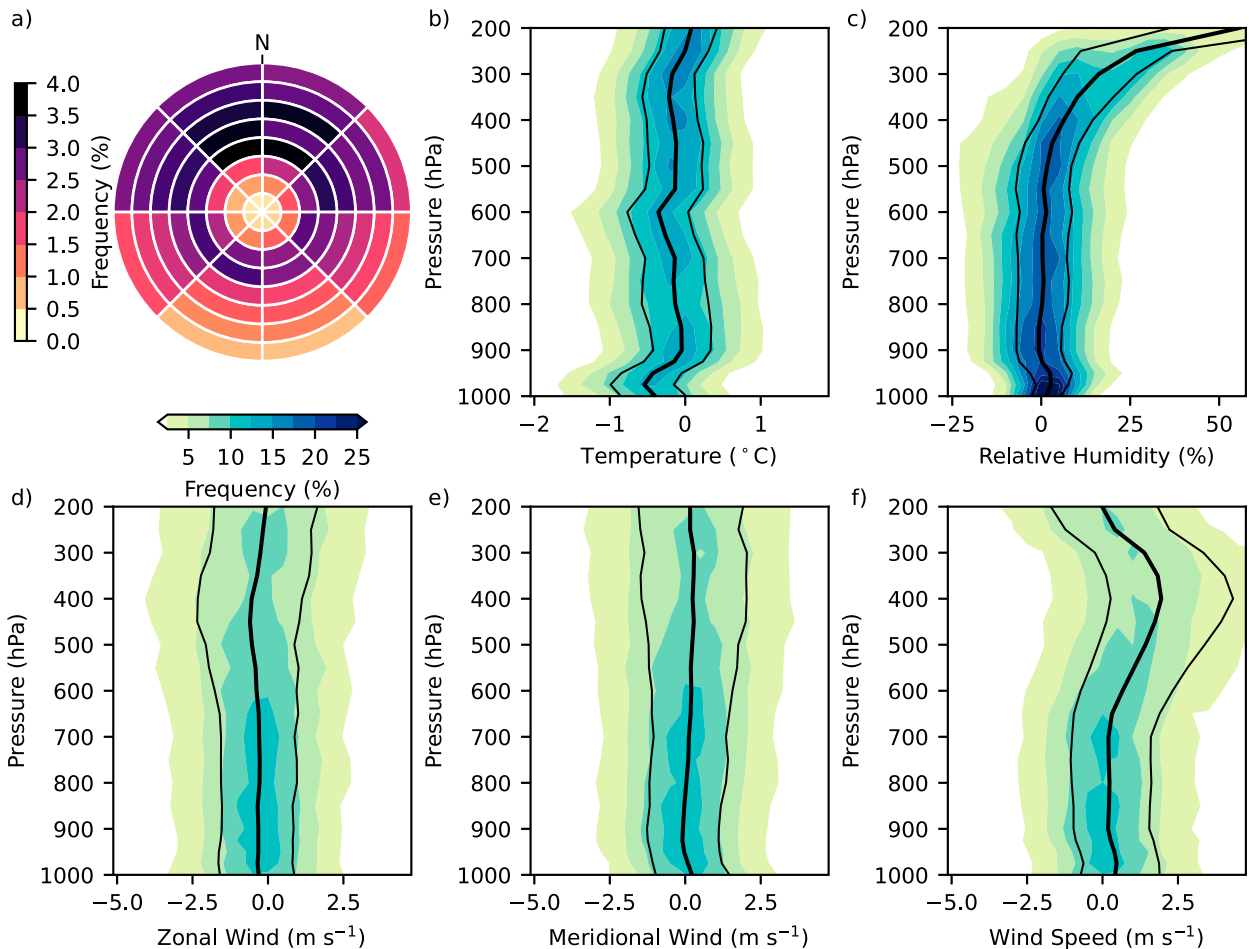
FIG. 8. Storm-relative comparison of the differences between ERA5 product output and nearly 7500 G-IV dropwindsonde observations during the 1998–2019 seasons released primarily in the North Atlantic with some releases in the central and eastern North Pacific. (a) The 100-km radius and 45° azimuth binned frequency of dropwindsonde launch locations out to 800 km relative to the storm center. The remaining panels are cumulative frequency by altitude diagrams that show shading of the binned frequency and the median (thick black curve) and the 25th and 75th percentiles of diagnostic quantities (thin black curves) for (b) temperature (in °C), (c) relative humidity (in %), (d) zonal wind (in m s^{-1}), (e) meridional wind (in m s^{-1}), and (f) wind speed (in m s^{-1}).

$f_1(t_1)$ and $f_2(t_2)$, we interpolate the values of the ERA5 fields to the dropsonde radius and azimuth location using a bivariate cubic spline. This smooth representation of the ERA5 fields will not reflect the values at the hourly analyses.

Figure 8a shows the frequency of dropwindsonde locations binned by 100-km radius and 45° azimuth. The remaining panels in Fig. 8 show cumulative frequency by altitude diagrams of the difference between ERA5 and the dropwindsondes for the 200–800-km (b) temperature and (c) relative humidity and for the 0–500-km (d) zonal and (e) meridional wind components as well as the (f) wind speed. While all fields are relatively low biased, a notable exception to the low bias is in the upper-level relative humidity where the moisture greatly exceeds observed values (Fig. 8c). For dropwindsondes, the fall speed and the slow response rate of the moisture sensor in cold temperatures of the upper-troposphere may contribute to the moist bias. But in other tropical regions, Ciesielski et al. (2014) shows the significant upper-tropospheric moist bias for

the Global Forecast System and Integrated Forecast System analyses as compared with radiosonde observations. In the lower troposphere below the trade inversion, the temperature field has a −0.5°C bias (Fig. 8b) that seems to be related to the moist bias shown in the relative humidity field. Ciesielski et al. (2014) shows a similar moisture bias in the boundary layer from the Integrated Forecast System in the north Indian Ocean. While not shown here, the ERA5 ocean surface temperature is consistent with the sea surface temperature products used in the SHIPS developmental dataset. This leads us to believe that the representation of boundary layer processes and trade inversion is contributing to these biases in the lowest levels of the modeled atmosphere around tropical cyclones.

To assess how these biases translate to the model diagnostic quantities, we conduct a similar analysis to the individual dropwindsonde composite analysis. However, we limit our analysis to G-IV flights that surround the storm. Here, we define "surround" to mean that there is at least one dropwindsonde
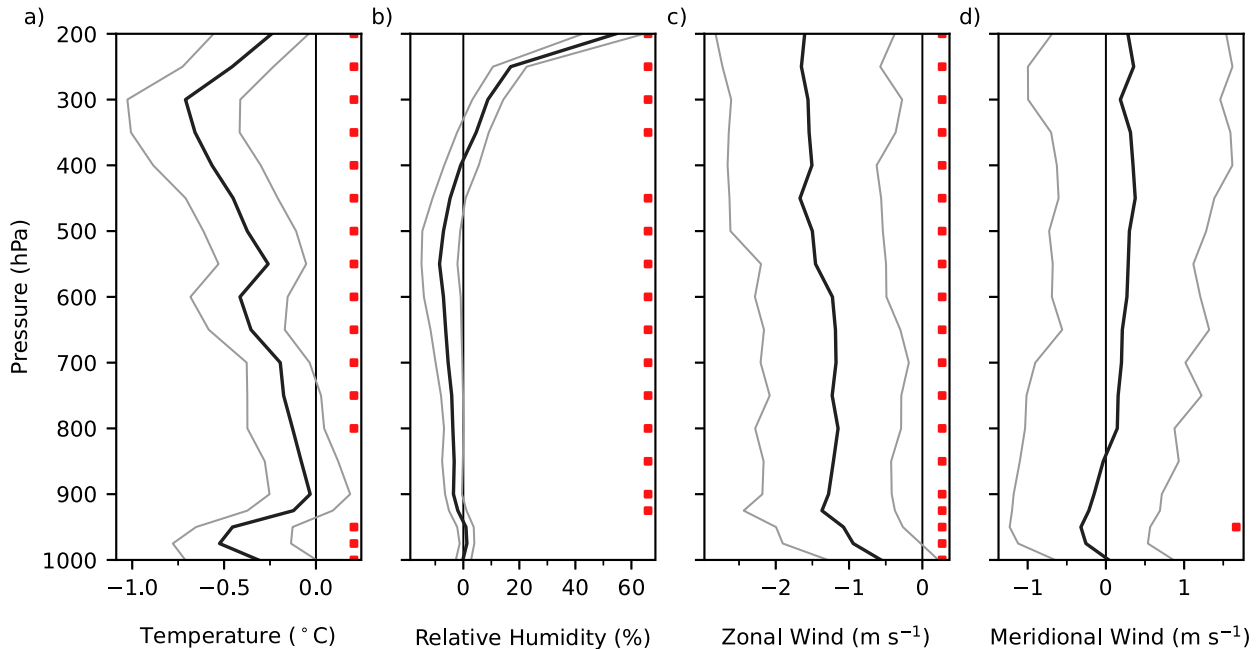
FIG. 9. A comparison of mean diagnostic profiles from ERA5 to 188 G-IV flights during the 1998–2019 North Atlantic and central and eastern North Pacific seasons. The flights have at least one dropwindsonde in each octant (45°) around and within 800 km of a time-interpolated storm position from which a mean profile is calculated from the octant average. Each panel shows the median (thick black curve) and the 25th and 75th percentiles of diagnostic quantities differences (thin gray curves) for the 200–800-km area-averaged (a) temperature (in °C) and (b) relative humidity (in %) as well as the 0–500-km area-averaged (c) zonal and (d) meridional components of the wind (in m s^{-1}). The red squares denote pressure levels where individual paired, two-sided Student's t tests with p values less than $\alpha_{\text{Walker}} = 1.322 \times 10^{-4}$ (i.e., we reject the null hypothesis).

per storm-centered octant (45°) within 800 km—a criterion that limits our analysis to 188 flights. We average the dropwindsondes in each octant and take the average of the octants to generate vertical profiles of temperature, relative humidity, and wind. While the dropwindsonde profiles under sample the areas represented by the model diagnostics, we repeat the same analysis in the paragraph above. Here, we use Eq. (10) to interpolate the ERA5 vertical profiles to the mean launch time of the dropwindsonde profile. Figure 9 shows the median and the 25th and 75th percentiles for the 200–800-km temperature and relative humidity and 0–500-km (c) zonal and (d) meridional wind components. Comparing Figs. 8 and 9, the deviations are largely the same, except for a −1 m s^{-1} zonal wind component bias in ERA5 that is not present in the individual dropwindsonde composite analysis. The bias increase in the zonal wind component shown in Fig. 9c are largely due to the subset representing midlatitude interactions. For the surrounding cases, we conduct a paired, two-sided Student's t test. We note that the kinematic and thermodynamic quantities are spatially correlated in the vertical and covarying. While the fields are not statistically independent, we use Walker's criterion, a stricter threshold for evaluating significance, to reduce the number of false rejections of the null hypothesis that the distribution of the dropwindsonde and ERA5 profiles at each pressure level are the same (Katz 2002; Wilks 2016). Walker's criterion is defined as $\alpha_{\text{Walker}} = 1 - (1 - \alpha_0)^{1/N_0} = 1.322 \times 10^{-4}$, where the overall significance level is $\alpha_0 = 0.01$, and the total

number of true null hypotheses is $N_0 = 76$ (19 levels and four fields). Figure 9 shows where we have rejected the null hypothesis with a red square and Table 3 shows the mean and standard deviation of the ERA5 profile and the bias relative to the dropwindsondes.

With diagnostic profile biases in mind, we calculate diagnostic quantities from the dropwindsonde profiles to compare with ERA5 and SHIPS. The left column of Fig. 10 shows scatterplots of the deep-layer and generalized shear calculated using (1) and (3) with ERA5 in blue and SHIPS in orange. The shear quantities for ERA5 (SHIPS) are highly correlated with Pearson correlation coefficients, r, of 0.85 (0.85) and 0.81 (0.82), respectively. For ERA5, the shear quantities exhibit a mean deviation of −0.4 and 0.0 kt, and standard deviations of 3.6 and 4.5 kt, respectively. SHIPS shows a positive bias in generalized shear in comparison to the dropwindsondes and ERA5, which is within the distribution shown of difference in Fig. 5 but with an opposite signal with respect to the median. The center column of Fig. 10 shows temperature gradient and advection with $r = 0.56$ (0.55) and 0.61 (0.65) for ERA5 (SHIPS). For the ERA5 temperature gradient comparison, the mean and standard deviation are -0.29×10^{-6} and 1.02×10^{-6} °C m^{-1}. For the ERA5 temperature advection comparison, the mean and standard deviation are 0.12×10^{-5} and 0.77×10^{-5} °C s^{-1}. With shear and temperature gradient and advection using the wind fields, the metrics are much more sensitive to the profile biases at low levels than the larger wind speeds near the tropopause.

TABLE 3. The vertical profiles of temperature, relative humidity, and u and v wind components for ERA5 for the 188 G-IV flights surrounding the tropical cyclone from 1998 to 2019 in the North Atlantic and eastern and central North Pacific. The mean and standard deviation (in parentheses) for ERA5 (roman) and the difference between ERA5 and the mean dropwindsondes (italics).

| Pressure (hPa) | Temperature (°C) | Relative humidity (%) | Wind | |
			u (m s^{-1})	v (m s^{-1})
200	−52.2 (1.2)	71.9 (11.2)	−1.44 (4.20)	3.62 (4.25)
	−0.3 (0.5)	*52.7 (15.4)*	*−1.58 (2.05)*	*0.35 (1.87)*
250	−40.2 (1.2)	61.6 (11.3)	−1.56 (3.77)	3.03 (4.11)
	−0.5 (0.5)	*16.1 (9.3)*	*−1.70 (1.82)*	*0.40 (2.00)*
300	−30.4 (1.1)	52.6 (12.0)	−1.73 (3.58)	2.21 (3.83)
	−0.8 (0.6)	*8.3 (9.0)*	*−1.47 (1.77)*	*0.36 (1.96)*
400	−15.6 (0.9)	46.9 (11.8)	−2.33 (3.22)	1.73 (2.76)
	−0.6 (0.5)	*−1.5 (9.3)*	*−1.59 (1.74)*	*0.44 (1.79)*
500	−5.4 (0.8)	50.1 (11.2)	−3.00 (2.97)	2.15 (2.18)
	−0.4 (0.4)	*−8.3 (9.6)*	*−1.54 (1.64)*	*0.26 (1.58)*
600	2.4 (0.7)	58.6 (9.9)	−3.42 (2.84)	2.72 (1.97)
	−0.4 (0.4)	*−7.3 (8.8)*	*−1.30 (1.52)*	*0.16 (1.61)*
700	9.7 (0.6)	61.9 (7.4)	−3.98 (2.74)	3.10 (2.05)
	−0.2 (0.3)	*−5.1 (6.5)*	*−1.23 (1.51)*	*0.06 (1.55)*
850	18.2 (0.8)	73.9 (4.5)	−4.82 (2.75)	3.08 (2.17)
	−0.1 (0.4)	*−3.6 (5.4)*	*−1.35 (1.52)*	*−0.10 (1.60)*
925	21.9 (1.1)	81.1 (4.4)	−5.25 (2.61)	2.21 (2.12)
	−0.1 (0.4)	*−1.8 (4.6)*	*−1.41 (1.53)*	*−0.26 (1.38)*
1000	26.6 (1.0)	79.9 (3.0)	−4.24 (1.81)	0.85 (1.53)
	−0.3 (0.6)	*−0.1 (4.1)*	*−0.41 (1.44)*	*0.09 (1.27)*

The right panel of Fig. 10 shows the convective mass flux for (a) the 0–500-km and (b) 200–800-km temperature and relative humidity profiles. The Pearson correlation coefficients between ERA5 (SHIPS) are 0.60 (0.41) and 0.56 (0.42), respectively. The convective mass flux from the ERA5 diagnostics has limited values on the upper end, suggesting that the model diagnostics may poorly resolve the environmental convective instability in comparison to the observations. This may be caused by the cold bias in the boundary layer shown in Figs. 8b and 9a. The convective mass flux in the SHIPS diagnostics has a similar slope to ERA5, but SHIPS captures higher convective mass flux values and shifts the distribution upward. This would indicate that SHIPS is more convectively favorable than ERA5. However, the convective mass flux in SHIPS also exhibits a weaker correlation to the dropwindsondes. While not shown here for other moisture and temperature quantities, the biases between ERA5 and SHIPS shown in Fig. 5 extrapolate to SHIPS and dropwindsondes (e.g., SHIPS has a positive moisture bias for RHLO, RHMD, and RHHI).

6. Discussion

Coupling the tropical cyclone with the large-scale environment has yielded and will continue to yield meaningful insight into stages of tropical cyclone evolution. To investigate tropical cyclone environmental measures, we discuss calculating the different variations with ERA5 that fall under the heading of SHIPS large-scale diagnostics. Here, we choose the so-called SHIPS model diagnostics variation to generate area-averaged vertical profiles of temperature, relative humidity, geopotential height, divergence, and relative vorticity as well as to calculate single-value quantities and diagnostics metrics

such as shear, temperature gradient and advection, and convective mass flux for global tropical cyclones that occurred during the 1998–2019 seasons. ERA5 supplies a consistent model at a fixed resolution, which is why we opt for the reanalysis when constructing TC PRIMED. However, a single source for diagnostic information can have systematic biases and does not address how well the reanalysis resolves diagnostic information. Also, these biases potentially impact how best to combine the information in TC PRIMED into an insightful analysis. Razin et al. (2022) provide an example use case for TC PRIMED by leveraging the shear vector to create a composite analysis of convection and precipitation that produces a result consistent with other tropical cyclone literature. However, new insight into tropical cyclone evolution may not benefit from prior literature, so ERA5's ability to resolve the tropical cyclone environment needs to be considered.

To understand the impact of these biases on resolving the tropical cyclone environment, we compare ERA5-based model diagnostics to the SHIPS developmental dataset. This comparison highlights that the kinematic fields (i.e., wind) do deviate—especially for the generalized wind shear in the Southern Hemisphere—but are relatively low biased. And, while position errors may cause some deviations, the center position induced uncertainty is within the uncertainty between SHIPS and ERA5. In the thermodynamic fields, we see that ERA5 has large biases relative to the SHIPS developmental dataset with ERA5 showing colder temperatures and higher moisture in the boundary layer and opposite biases in the free atmosphere. The differences in the thermodynamic fields are large relative to kinematic quantities, which translate to ERA5 being less convectively active than the source models used for SHIPS.
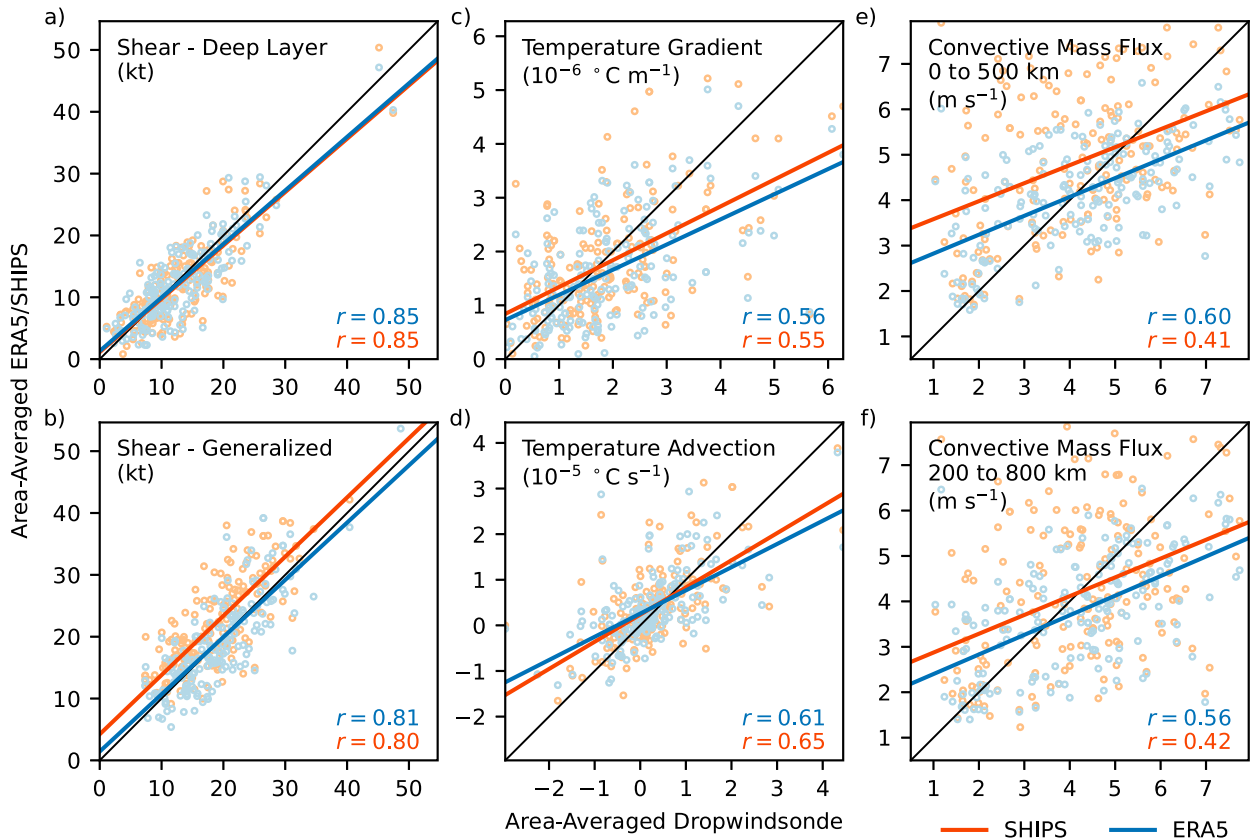
FIG. 10. Scatterplots of diagnostic metrics calculated from the area-averaged dropwindsonde (abscissa) and model-based diagnostics (ordinate) for (a) 0–500-km deep-layer vertical wind shear, (b) 0–500-km generalized wind shear, (c) 0–500-km 700–850-hPa temperature gradient, (d) 0–500-km 700–850-hPa temperature advection, and convective mass flux calculated from temperature and relative humidity with an entrained plume model for (e) 0–500 km and (f) 200–800 km. Each panel shows the one-to-one line (thin black curve), least squares regression (thick blue curve for ERA5 and orange curve for SHIPS) with r, the Pearson correlation coefficient, and scatter points (light blue for ERA5 and light orange for SHIPS).

While the comparison between two model-based diagnostics is useful, it does not address our question about how well ERA5 captures the synoptic-scale supporting structure around tropical cyclones. To quantify biases, we use dropwindsondes, which are mainly available in the North Atlantic with occasional releases in the eastern and central North Pacific. In conducting the analysis two ways with individual and storm-surrounding dropwindsonde profiles, we see that ERA5 is relatively low biased in kinematic and thermodynamic fields. Across fields, the trade inversion stands out with biases in the boundary layer. In the upper troposphere, the model shows a moist bias aloft that Ciesielski et al. (2014) has documented in the operational Integrated Forecast System and Global Forecast System. In looking at derived quantities, ERA5-based shear diagnostic metrics compare well to observations. The temperature gradient and advection—low-level wind-derived metrics—show larger biases, suggesting that the vertical variations of low-level winds are not as accurate. However, SHIPS also shows a similar signature, which may suggest that the resolution of global models cannot resolve the observed variability. For temperature and relative humidity, we assess convective instability with an entrained plume

model, and we note that the large-scale tropical cyclone environment in ERA5 misses the upper end of the convective instability distribution. This may be caused by the cold bias in the boundary layer. The combination of the cold, moist boundary layer and dry free atmosphere creates an environmental pattern similar to the impact of daytime-only solar radiation experiments on the tropical free atmosphere (Melhauser and Zhang 2014). While ERA5 is less convectively active, the convective mass flux calculated from ERA5 has a higher correlation to observations than the SHIPS developmental dataset, which suggest that the convective activity is more of a systematic bias.

Unfortunately, our comparison of ERA5 to the Gulfstream IV-SP dropwindsondes is confined primarily to the North Atlantic with some eastern and central North Pacific cases. The North Atlantic has a greater density of observations, which does make it challenging to extrapolate our North Atlantic findings globally. The comparison between ERA5 and SHIPS does however suggest that other basins, and particularly the Southern Hemisphere, show larger variability. This raises some questions. Is the observed large-scale environmental variability related to the number and quantity of observations? Are

the number of observations available in some basin inadequate for resolving tropical cyclones in reanalyses? In addition, the analysis shows that there is greater global interannual variability, which could be related to true interannual variability or may reflect biases associated with upgrades of the GFS analyses and mix of GFS analyses and CFSR used in creating the SHIPS developmental dataset. We hope to determine the causes of this environmental variability in future work.

Using large-scale diagnostic metrics calculated from a single source, like ERA5, is important because we can identify and isolate the impact of systematic biases. However, it is equally important to know the uncertainty in the environmental metrics. Here, we framed quantifying this as "Does ERA5 mark a new era for resolving the tropical cyclone environment?" As shown, the ERA5 product performance in resolving the synoptic-scale supporting structure is diagnostic metric specific, which is important to consider when conducting metric-dependent analyses as demonstrated by the shear-relative composites in section 4 of Razin et al. (2022). Through this analysis, we attempt to capture and convey the ability of ERA5 to resolve the large-scale environment by providing uncertainty context to aid users of TC PRIMED or other sources of diagnostic metrics.

Data availability statement. The information about the CIRA/RAMMB TC PRIMED (Razin et al. 2022a) is on the project page at https://rammb-data.cira.colostate.edu/tcprimed/ and the dataset is available at https://doi.org/10.25921/dmy1-0595. The ERA5 products used here and in TC PRIMED are generated using and contains modified Copernicus Climate Change Service information (updated 2020; Hersbach et al. 2018a,b) and neither the European Commission nor ECMWF is responsible for any use that may be made of the Copernicus information or data it contains. The CIRA/RAMMB SHIPS developmental dataset can be found at https://rammb.cira.colostate.edu/research/tropical_cyclones/ships/developmental_

data.asp. The NOAA Hurricane Research Division dropwindsonde data archive is located at https://www.aoml.noaa.gov/hrd/data_sub/dropsonde.html.

REFERENCES

Aberson, S. D., and J. L. Franklin, 1999: Impact on hurricane track and intensity forecasts of GPS dropwindsonde observations from the first-season flights of the NOAA Gulfstream-IV jet aircraft. *Bull. Amer. Meteor. Soc.*, **80**, 421–428, https://doi.org/10.1175/1520-0477(1999)080<0421:IOHTAI>2.0.CO;2.

Barnes, S. L., 1964: A technique for maximizing details in numerical weather map analysis. *J. Appl. Meteor.*, **3**, 396–409, https://doi.org/10.1175/1520-0450(1964)003<0396:ATFMDI>2.0.CO;2.

Byrd, R. H., P. Lu, J. Nocedal, and C. Zhu, 1995: A limited memory algorithm for bound constrained optimization. *SIAM J. Sci. Comput.*, **16**, 1190–1208, https://doi.org/10.1137/0916069.

Ciesielski, P. E., P. T. Haertel, R. H. Johnson, J. Wang, and S. M. Loehrer, 2012: Developing high-quality field program sounding datasets. *Bull. Amer. Meteor. Soc.*, **93**, 325–336, https://doi.org/10.1175/BAMS-D-11-00091.1.

——, and Coauthors, 2014: Quality-controlled upper-air sounding dataset for DYNAMO/CINDY/AMIE: Development and corrections. *J. Atmos. Oceanic Technol.*, **31**, 741–764, https://doi.org/10.1175/JTECH-D-13-00165.1.

Combot, C., A. Mouche, J. Knaff, Y. Zhao, Y. Zhao, L. Vinour, Y. Quilfen, and B. Chapron, 2020: Extensive high-resolution Synthetic Aperture Radar (SAR) data analysis of tropical cyclones: Comparisons with SFMR flights and best track. *Mon. Wea. Rev.*, **148**, 4545–4563, https://doi.org/10.1175/MWR-D-20-0005.1.

Davis, C. A., 2018: Resolving tropical cyclone intensity in models. *Geophys. Res. Lett.*, **45**, 2082–2087, https://doi.org/10.1002/2017GL076966.

DeMaria, M., 2009: A simplified dynamical system for tropical cyclone intensity prediction. *Mon. Wea. Rev.*, **137**, 68–82, https://doi.org/10.1175/2008MWR2513.1.

——, and J. Kaplan, 1994: A Statistical Hurricane Intensity Prediction Scheme (SHIPS) for the Atlantic basin. *Wea. Forecasting*, **9**, 209–220, https://doi.org/10.1175/1520-0434(1994)009<0209:ASHIPS>2.0.CO;2.

——, M. Mainelli, L. K. Shay, J. A. Knaff, and J. Kaplan, 2005: Further improvements to the Statistical Hurricane Intensity Prediction Scheme (SHIPS). *Wea. Forecasting*, **20**, 531–543, https://doi.org/10.1175/WAF862.1.

Dorst, N. M., 2007: The National Hurricane Research Project: 50 years of research, rough rides, and name changes. *Bull. Amer. Meteor. Soc.*, **88**, 1566–1588, https://doi.org/10.1175/BAMS-88-10-1566.

Dunion, J. P., 2011: Rewriting the climatology of the tropical North Atlantic and Caribbean Sea atmosphere. *J. Climate*, **24**, 893–908, https://doi.org/10.1175/2010JCLI3496.1.

Elsberry, R. L., and R. A. Jeffries, 1996: Vertical wind shear influences on tropical cyclone formation and intensification during TCM-92 and TCM-93. *Mon. Wea. Rev.*, **124**, 1374–1387, https://doi.org/10.1175/1520-0493(1996)124<1374:VWSIOT>2.0.CO;2.

Frank, W. M., 1977: The structure and energetics of the tropical cyclone I. Storm structure. *Mon. Wea. Rev.*, **105**, 1119–1135, https://doi.org/10.1175/1520-0493(1977)105<1119:TSAEOT>2.0.CO;2.

Gray, W. M., 1979: Hurricanes: Their formation, structure and likely role in the tropical circulation. *Meteorology over the Tropical Oceans*, D. B. Shaw, Ed., Royal Meteorological Society, 155–218.

Hersbach, H., and D. Dee, 2016: ERA5 reanalysis is in production. *ECMWF Newsletter*, No. 147, ECMWF, Reading, United Kingdom, 7 pp., http://www.ecmwf.int/sites/default/files/elibrary/2016/16299-newsletter-no147-spring-2016.pdf.

——, and Coauthors, 2018a: ERA5 hourly data on pressure levels from 1979 to present. Copernicus Climate Change Service (C3S) Climate Data Store (CDS), accessed 20 July 2020, https://doi.org/10.24381/cds.bd0915c6.

——, and Coauthors, 2018b: ERA5 hourly data on single levels from 1979 to present. Copernicus Climate Change Service (C3S) Climate Data Store (CDS), accessed 20 July 2020, https://doi.org/10.24381/cds.adbb2d47.

——, and Coauthors, 2020: The ERA5 global reanalysis. *Quart. J. Roy. Meteor. Soc.*, **146**, 1999–2049, https://doi.org/10.1002/qj.3803.

Hill, K. A., and G. M. Lackmann, 2009: Influence of environmental humidity on tropical cyclone size. *Mon. Wea. Rev.*, **137**, 3294–3315, https://doi.org/10.1175/2009MWR2679.1.

Hock, T. F., and J. L. Franklin, 1999: The NCAR GPS dropwindsonde. *Bull. Amer. Meteor. Soc.*, **80**, 407–420, https://doi.org/10.1175/1520-0477(1999)080<0407:TNGD>2.0.CO;2.

Hodges, K., A. Cobb, and P. L. Vidale, 2017: How well are tropical cyclones represented in reanalysis datasets? *J. Climate*, **30**, 5243–5264, https://doi.org/10.1175/JCLI-D-16-0557.1.

Kalnay, E., 2003: *Atmospheric Modeling, Data Assimilation and Predictability.* Cambridge University Press, 341 pp.

Katz, R. W., 2002: Sir Gilbert Walker and a connection between El Niño and statistics. *Stat. Sci.*, **17**, 97–112, https://doi.org/10.1214/ss/1023799000.

Knaff, J. A., C. R. Sampson, and M. DeMaria, 2005: An operational statistical typhoon intensity prediction scheme for the western North Pacific. *Wea. Forecasting*, **20**, 688–699, https://doi.org/10.1175/WAF863.1.

——, ——, and K. D. Musgrave, 2018: An operational rapid intensification prediction aid for the western North Pacific. *Wea. Forecasting*, **33**, 799–811, https://doi.org/10.1175/WAF-D-18-0012.1.

Landsea, C. W., and J. L. Franklin, 2013: Atlantic hurricane database uncertainty and presentation of a new database format. *Mon. Wea. Rev.*, **141**, 3576–3592, https://doi.org/10.1175/MWR-D-12-00254.1.

Maclay, K. S., M. DeMaria, and T. H. Vonder Haar, 2008: Tropical cyclone inner-core kinetic energy evolution. *Mon. Wea. Rev.*, **136**, 4882–4898, https://doi.org/10.1175/2008MWR2268.1.

Marchok, T., 2002: How the NCEP tropical cyclone tracker works. Preprints, *25th Conf. on Hurricanes and Tropical Meteorology*, San Diego, CA, Amer. Meteor. Soc., JP1.13, http://ams.confex.com/ams/pdfpapers/37628.pdf.

——, 2021: Important factors in the tracking of tropical cyclones in operational models. *J. Appl. Meteor. Climatol.*, **60**, 1265–1284, https://doi.org/10.1175/JAMC-D-20-0175.1.

McNoldy, B. D., M. DeMaria, V. Tallapragada, and T. Marchok, 2010: HWRF performance diagnostics from the 2009 Atlantic hurricane season. Preprints, *29th Conf. on Hurricanes and Tropical Meteorology*, Tucson, AZ, Amer. Meteor. Soc., JP1.63, https://ams.confex.com/ams/pdfpapers/167993.pdf.

Melhauser, C., and F. Zhang, 2014: Diurnal radiation cycle impact on the pregenesis environment of Hurricane Karl (2010). *J. Atmos. Sci.*, **71**, 1241–1259, https://doi.org/10.1175/JAS-D-13-0116.1.

Ooyama, K. V., 1969: Numerical simulation of the life cycle of tropical cyclones. *J. Atmos. Sci.*, **26**, 3–40, https://doi.org/10.1175/1520-0469(1969)026<0003:NSOTLC>2.0.CO;2.

——, 1982: Conceptual evolution of the theory and modeling of the tropical cyclone. *J. Meteor. Soc. Japan*, **60**, 369–380, https://doi.org/10.2151/jmsj1965.60.1_369.

——, 1990: A thermodynamic foundation for modeling the moist atmosphere. *J. Atmos. Sci.*, **47**, 2580–2593, https://doi.org/10.1175/1520-0469(1990)047<2580:ATFFMT>2.0.CO;2.

RAMMB, 2022: SHIPS Developmental Dataset. Regional and Mesoscale Meteorology Branch (RAMMB), Cooperative Institute for Research in the Atmosphere, accessed 1 May 2020, https://rammb.cira.colostate.edu/research/tropical_cyclones/ships/.

Razin, M. N., C. J. Slocum, J. A. Knaff, and P. J. Brown, 2022a: Tropical Cyclone Precipitation, Infrared, Microwave, and Environmental Dataset (TC PRIMED), version 1.0, NOAA National Centers for Environmental Information, accessed 20 July 2020, https://doi.org/10.25921/dmy1-0595.

——, ——, ——, ——, and M. M. Bell, 2022b: Tropical cyclone precipitation, infrared, microwave, and environmental database. *Bull. Amer. Meteor. Soc.*, https://doi.org/10.1175/BAMS-D-21-0052.1, in press.

Ryan, K., L. Bucci, J. Delgado, R. Atlas, and S. Murillo, 2019: Impact of Gulfstream-IV dropsondes on tropical cyclone prediction in a regional OSSE system. *Mon. Wea. Rev.*, **147**, 2961–2977, https://doi.org/10.1175/MWR-D-18-0157.1.

Sampson, C. R., and A. J. Schrader, 2000: The Automated Tropical Cyclone Forecasting System (version 3.2). *Bull. Amer. Meteor. Soc.*, **81**, 1231–1240, https://doi.org/10.1175/1520-0477(2000)081<1231:TATCFS>2.3.CO;2.

Schumacher, A. B., M. DeMaria, and J. A. Knaff, 2009: Objective estimation of the 24-h probability of tropical cyclone formation. *Wea. Forecasting*, **24**, 456–471, https://doi.org/10.1175/2008WAF2007109.1.

Simpson, J., and V. Wiggert, 1969: Models of precipitating cumulus towers. *Mon. Wea. Rev.*, **97**, 471–489, https://doi.org/10.1175/1520-0493(1969)097<0471:MOPCT>2.3.CO;2.

Stern, D. P., G. H. Bryan, and S. D. Aberson, 2016: Extreme low-level updrafts and wind speeds measured by dropsondes in tropical cyclones. *Mon. Wea. Rev.*, **144**, 2177–2204, https://doi.org/10.1175/MWR-D-15-0313.1.

Torn, R. D., and C. Snyder, 2012: Uncertainty of tropical cyclone best-track information. *Wea. Forecasting*, **27**, 715–729, https://doi.org/10.1175/WAF-D-11-00085.1.

Velden, C. S., and J. Sears, 2014: Computing deep-tropospheric vertical wind shear analyses for tropical cyclone applications: Does the methodology matter? *Wea. Forecasting*, **29**, 1169–1180, https://doi.org/10.1175/WAF-D-13-00147.1.

Vömel, H., K. Young, and T. Hock, 2016: NCAR GPS dropsonde humidity dry bias. NCAR Tech. Note NCAR/TN-531+STR, 8 pp, https://doi.org/10.5065/D6XS5SGX.

Wilks, D. S., 2016: "The stippling shows statistically significant grid points": How research results are routinely overstated and over-interpreted, and what to do about it. *Bull. Amer. Meteor. Soc.*, **97**, 2263–2273, https://doi.org/10.1175/BAMS-D-15-00267.1.

Winterbottom, H. R., and E. P. Chassignet, 2011: A vortex isolation and removal algorithm for numerical weather prediction model tropical cyclone applications. *J. Adv. Model. Earth Syst.*, **3**, M11003, https://doi.org/10.1029/2011MS000088.

Zipser, E. J., 2003: Some views on "hot towers" after 50 years of tropical field programs and two years of TRMM data. *Cloud Systems, Hurricanes, and the Tropical Rainfall Measuring Mission, Meteor. Monogr.*, No. 51, Amer. Meteor. Soc., 49–58, https://doi.org/10.1007/978-1-878220-63-9_5.